August 2014

Novel Substrate-Bound Hybrid Nanomaterials for Anode Electrodes in Lithium-Ion Batteries

Haejune Kim
University of Wisconsin-Milwaukee

Recommended Citation

Kim, Haejune, "Novel Substrate-Bound Hybrid Nanomaterials for Anode Electrodes in Lithium-Ion Batteries" (2014). *Theses and Dissertations*. 707.
https://dc.uwm.edu/etd/707

NOVEL SUBSTRATE-BOUND HYBRID NANOMATERIALS FOR ANODE ELECTRODES IN LITHIUM-ION BATTERIES

by

Haejune Kim

A Dissertation submitted in
Partial Fulfillment of the
Requirements for the Degree of

Doctor of Philosophy
In Engineering

at
The University of Wisconsin-Milwaukee
August 2014

ABSTRACT

NOVEL SUBSTRATE-BOUND HYBRID NANOMATERIALS FOR ANODE ELECTRODES IN LITHIUM-ION BATTERIES

by

Haejune Kim

The University of Wisconsin-Milwaukee, 2014
Under the Supervision of Professor Junhong Chen

Li-ion batteries (LIBs) are commercially dominant in electrochemical energy storage devices. Their wide applications as power sources, from portable electronics to electric vehicles/hybrid electric vehicles, are mainly attributed to their superior energy density based on unit volume and unit weight over other battery systems. Growing demands for lighter, longer-lasting, and more powerful devices spur the development of new electrode materials, because the performance of LIBs is highly dependent on the characteristics of electrodes. The ideal candidate for anode materials of LIBs should have high lithium storage capability and stable structure after repeated charge/discharge cycles. Since its first commercialization by Sony Corporation in 1991, graphite has been the most popular anode material in LIBs because of its abundance, decent reversible energy capacity, and good electrochemical stability within a wide potential range. However,

current LIB technology using graphite-based anode has reached its performance limit due to the constraints by the theoretical specific capacity (372 mAh/g) of graphite. Silicon is one of the most promising anode materials for LIBs to replace conventional graphite anodes due to its highest theoretical capacity of 3,579 mAh/g. However, a substantial volume expansion/contraction of silicon during the lithiation/de-lithiation cycles typically leads to the loss of electrical contact between the silicon materials and the current collector, causing shortened battery life and poor battery performance. It is thus highly desirable to design new electrodes that can survive the large volume change over the extended cycle life without significant degradation.

The objective of this research is to explore new hybrid materials containing silicon thin films (active materials) and substrate-bound carbon nanostructures (less active supporting matrix) as an anode for LIBs. The resulting hybrid anode materials inherit both unique properties of the Si films (e.g., high lithium storage capacity) and those of the substrate-bound structure (e.g., strong adhesion to the current collector, good electrical conductivity). The direct growth of supporting matrix on a current collector without any additives results in strong adhesion to the substrate to ensure a stable cycle life. Instead of using catalysts to grow the supporting matrix, various carbon nanostructures including carbon nanofibers (CNFs) and highly branched graphene nanosheets (HBGNs) are grown directly on the current collector and integrated with Si films.

All the hybrid materials grown on the current collector are directly used for an anode without further processing. The binder- and conductive additive-free electrodes eliminate the deadweight loss, and thus increase the specific energy density in the battery system. The hybrid Si/HBGN exhibits a good cycle performance with proper control of the loading density and the thickness of the Si film. The void space in HBGNs plays a critical role in the electrochemical performance to accommodate the strain relief of the Si film. The hybrid Si/CNF provides a facile approach to produce Si- and carbon-based hybrid electrodes by modifying the current collector to favor Si film deposition. The poor capacity retention of Si electrodes is effectively addressed by combining the advantageous features of CNFs and Si film. The hybrid CNF/HBGN provides a continuous conduction pathway, which is expected to lead to a high charge carrier mobility. The hybrid CNF/HBGN as an anode material has a higher Li storage capability compared with CNF alone. The HBGNs with nanoporous cavities, large surface area, and edges of exposed graphene platelets provide more sites for Li-ion storage.

Based on this study, we conclude that the substrate-bound carbon nanostructures in the hybrid provide a strong mechanical support for long cycle life and a large surface area for a high loading density of active materials, while Si thin films offer a high Li storage capacity. By conducting systematic studies on the different types of substrate-bound carbon nanostructured electrodes, this study contributes to the development of novel anodes in LIBs. It is anticipated that this study will lead to an efficient route to fabricating high-performance binder- and conductive additive-free anode electrodes for next-generation LIBs.

TABLE OF CONTENTS

LIST OF FIGURES

LIST OF TABLES

LIST OF ABBREVIATIONS

0D	zero-dimensional
1D	one-dimensional
2D	two-dimensional
3D	three-dimensional
BET	Brunauer–Emmett–Teller
CNT	carbon nanotube
CNF	carbon nanofiber
CVD	chemical vapor deposition
EDS	energy-dispersive X-ray spectroscopy
EV	electric vehicle
GO	graphene oxide
HBGN	highly branched graphene nanosheet
HEV	hybrid electric vehicle
LIB	lithium-ion battery
MWCNT	multiwalled carbon nanotube
NP	nanoparticle

NW	nanowire
PECVD	plasma-enhanced chemical vapor deposition
SAED	selected area electron diffraction
SEM	scanning electron microscopy
TEM	transmission electron microscopy
XRD	X-ray diffraction

CHAPTER 1 INTRODUCTION AND RESEARCH OBJECTIVES

1.1. Introduction to Lithium-Ion Batteries

Lithium-ion batteries (LIBs) have attracted considerable attention as next-generation secondary batteries mainly due to their high energy density based on unit volume and weight. Modern Li-ion 18650 cells hold about 250 Wh/kg and 650 Wh/L which increased more than double the energy capacity of its first commercialized cells two decades ago. In addition, LIBs do not lose their capacity over time by incomplete charge/discharge, which is known as "the memory effect" that usually occurs for nickel-cadmium and nickel-metal hydride batteries. The first commercialized LIB-C/$LiCoO_2$[1] was developed by Sony Corporation in 1991 and has been widely used as a rechargeable power source for portable electronics such as tablets, digital cameras, e-book readers, laptop computers, cellular phones and many other portable devices. LIBs are also considered as a practical solution for powering electric vehicles (EVs) and hybrid electric vehicles (HEVs).

What makes LIBs so popular in energy storage systems? It is important to understand how LIBs work to find out the answer. Typically, an LIB consists of a cathode, an anode, a separator, and an electrolyte, as shown in Figure 1.1. The performance of an LIB mainly depends on the characteristics of electrodes and electrolytes. The most commonly used electrode materials for commercial LIBs are lithium cobalt oxide (cathode) and graphite (anode). A slurry spread method is used to prepare conventional electrodes by coating the current collector (typically copper for an anode and aluminum for a cathode) with a slurry mixture of active electrode materials, conductive additives, and a polymeric binder.

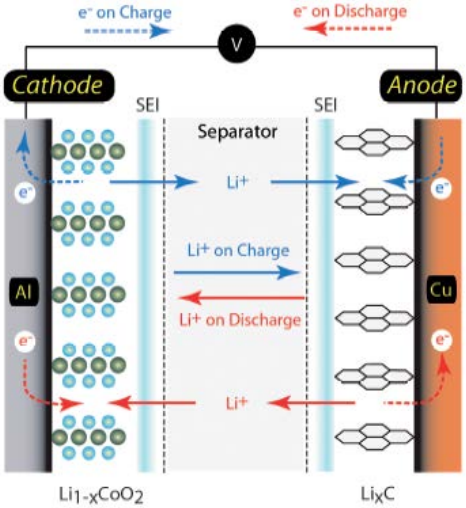

Figure 1.1 Schematic illustration of electron and ion flows during charge/discharge processes in LIBs.[2] The Li-ions flow back and forth between $LiCoO_2$ (cathode) and graphitic carbon (anode) through an ionically conducting electrolyte. The electrons move through a closed external circuit.

The conductive additives such as carbon black and acetylene black are added in the slurry to improve the electrical conductivity. The binder is used to physically bond the active materials to the current collector for better electrical contact. The electrolyte is an ionically conductive material that does not allow the electron transfer. During charge/discharge processes, Li-ions flow between the positive electrode (cathode) and the negative electrode (anode) through the electrolyte solution. The Li-ions are supplied by the cathode, typically a lithium-containing transition metal oxide ($LiCoO_2$, $LiMn_2O_4$) or transition metal phosphates ($LiFePO_4$, $LiMnPO_4$). During charging, Li-ions from the cathode are de-intercalated and intercalated into the anode while electrons flow from the positive electrode to the negative electrode to balance the charges between the two electrodes. The reverse of this process happens during discharging. Li-ions flow from the anode to the cathode through the electrolyte and electrons flow through the external load of resistance. The following is a list of typical reduction-oxidation (redox) reactions occurring in an LIB.

Positive electrode: $LiMO_2 \rightarrow Li_{1-x}MO_2 + xLi^+ + xe^-$

Negative electrode: $C + xLi^+ + xe^- \rightarrow Li_xC$

Overall : $LiMO_2 + C \rightleftarrows Li_xC + Li_{1-x}MO_2$

where M is a transitional metal such as Mn, Ni, or Co. Lithium can be abundantly supplied from sea water.[3] In fact, pure lithium metal was initially used as an anode material because metallic lithium provides a high theoretical capacity of 3,862 mAh/g and a low density of 0.53 g/cm^3, as well as a low standard potential of -3.045 V.[4] But it posed serious safety concerns due to the deposition of lithium dendrites that could lead to a short circuit and an explosion of the cells. The ideal candidate for the anode materials of LIBs should have such characteristics as high lithium storage capacity and flawless structure after repeated charge/discharge cycles.

The graphite as a host material in the anode shows excellent cycling behavior; however, its limited energy capacity (theoretical value: 372 mAh/g, corresponding to LiC_6) does not satisfy today's demands for a higher energy density and power rate of energy storage systems. In recent years, several automotive companies have employed LIBs to provide electrical propulsion in EVs such as Renault Fluence, Nissan Leaf, Chevrolet Volt, and Tesla Roadster. These EVs rely on low energy density LIBs based on carbon-anode electrodes; however, it is a dilemma to use such heavy and large battery cells. Indeed, new anode materials with a high energy density are critically needed to fulfill today's high needs.

The electrochemical processes in LIBs follow thermodynamic laws. The reaction in the electrochemical cells can be described as follows:

$$aA + ne^- \rightleftarrows cC$$

$$bB - ne^{-} \rightleftarrows dD$$

where a, b, and c, d are moles of reactants (A, B) and products (C, D), respectively. n is number of electrons per mole of reactant.[5] The overall reaction can be described as,

$$aA + bB \rightleftarrows cC + dD$$

The electrical work (W) can be produced by the chemical potential difference between the cathode and the anode or the change of Gibbs free energy in standard form.

$$W = \Delta G = -nFE \qquad \text{Eq. (1.1)}$$

or

$$\Delta G^{0} = -nFE - \frac{nRT}{F} ln \frac{(aC)^{c}(aD)^{d}}{(aA)^{a}(aB)^{b}} \qquad \text{Eq. (1.2)}$$

where F is a Faraday constant. This equation is useful to determine the theoretical energy capacity provided by a system.

It is important to know the diffusion process of Li-ions to evaluate the power performance of LIBs. During charge/discharge processes, Li-ions diffuse back and forth through the electrolyte. The mobility of electrons is much higher than that of Li-ions.[6] Therefore, the reaction rate is strongly dependent on the diffusion rate of Li-ions. The internal resistance in the battery originates from the ion transport in the electrolyte, the interface between the electrolyte and the active materials, and within the active materials. The kinetics of the Li-ion intercalation/de-intercalation can be determined by AC impedance spectroscopy.

1.2. Literature Review on Nanostructured Electrode Materials

Next-generation LIBs should be equipped with high energy/power density, good safety, and a long cycle life. The performance of LIBs greatly depends on the characteristics of electrode materials. The purpose of this research is to develop new anode materials that have the following characteristics:

- low potential of lithium insertion and extraction versus lithium
- high capacity of storing lithium
- durable structure after long repeated charge and discharge cycles
- environmentally friendly materials
- facile fabrication method for mass production
- low cost
- high Li^+ diffusivity for high power density

With substantial progress in nanotechnology, nanostructured materials have shown several advantages over bulk materials, including an effective strain accommodation and a short Li-diffusion path. The short Li-diffusion distance in nanoscale materials significantly increases the rate performance of the battery according to the following relation:

$$\tau = L^2/D \qquad \text{Eq. (1.3)}$$

where τ is the characteristic time for diffusion, L is the Li-ion diffusion length and D is the diffusion coefficient.[7] Moreover, large surface area of the nanomaterials increases the interface area between the electrolytes and the active materials, thereby leading to a high Li-ion flux.

A variety of nanomaterials have been studied as anode materials for LIBs, including C, Si, Sn, Sb, Al, Mg, and Ge. We compare the material properties of selected elements in Table 1.1. Among those elements, Si shows the most outstanding properties for use as anode materials. Si has the highest theoretical specific capacity when the Si-Li alloy forms $Li_{15}Si_4$. Besides, it is abundant in the Earth’s crust, environmentally benign, and inexpensive. In this review, we highlight the electrochemical performance of nanostructured carbon (CNT and graphene), Li-alloy metal (Si) and Si/C hybrids for anode materials in LIBs.

Table 1.1 Comparison of material properties of various anode materials in LIBs.

Materials	**Li**	**C**	**Si**	**Sn**	**Sb**	**Al**	**Mg**	**Ge**
Density (g cm^{-3})	0.53	2.25	2.33	7.29	6.7	2.7	1.3	5.5
Lithiated phase	Li	LiC_6	$Li_{15}Si_4$	$Li_{4.4}Sn$	Li_3Sb	LiAl	Li_3Mg	$Li_{15}Ge_4$
Theoretical specific capacity (mA h g^{-1})	3,862	372	3,579	994	660	993	3,350	1,624
Theoretical charge density (mA h cm^{-3})	2,047	837	9,786	7,246	4,422	2,681	4,355	7,366
Volume change (%)	100	12	280	260	200	96	100	370
Potential vs. Li (V)	0	0.05	0.4	0.6	0.9	0.3	0.1	0.4

Nanocarbon-based anode materials

Carbon in the form of natural and synthetic graphite, carbon black, and carbon fibers are the most commonly used materials in LIBs. The electrochemical properties of carbon are strongly related to the morphology, crystallinity, and orientation of the crystallites.[8] Carbon can be classified as graphite, soft carbon, and hard carbon. Graphite is a layered compound with ABAB stacking order of graphene. Soft carbon refers to highly ordered carbon, while hard carbon is a highly disordered carbon. With the advent of nanotechnology, novel materials such as mesocarbon microbeads (MCMB), carbon nanotubes (CNTs), graphene, and carbon-based composites have been synthesized for anode applications. MCMB has been widely used in commercial LIBs due to its good cyclability at a low charge/discharge rate[9]; however it has a very low reversible capacity of 230 mAh/g at a 1 C rate.[10]

Since the report on electrochemical energy storage of CNTs,[11] researchers are actively investigating on the use of carbon nanotubes for the application in LIBs. The CNTs have excellent mechanical and electronic properties with good lithium storage capability,[12, 13] which not only can be used as host materials of Li-ions, but can also serve as a building block in composite materials. The CNTs provide various Li-storage sites such as the large surface area, the interstitial sites within the CNT bundles, and the interspacing between graphene layers. In addition, Li-ions can diffuse through the open end or topological defects of the CNTs. However, the first Coulombic efficiency (CE: discharge capacity/charge capacity $\times 100$) of raw CNTs was very low (~30%) [14] and had high voltage hysteresis during charge/discharge processes.[15] This irreversible capacity (charge capacity-discharge capacity) is attributed to the reductive decomposition of the electrolyte, which forms a solid-electrolyte interphase (SEI) film on the carbonaceous anode material. The formation of the SEI film usually occurs in the first few cycles of charge/discharge.

The CNTs as anode materials can be prepared via various synthetic procedures such as arc discharge,[16] laser ablation,[17] and chemical vapor deposition.[18] Yang et al. reported that the electrochemical performance of CNTs was greatly affected by their morphology, structure, and synthesis method.[19] Their results showed that the electrochemical properties of CNTs can be improved by an acid oxidation treatment, creating structural defects along the sidewalls of CNTs. Gao et al. also reported that topological defects by the mechanical ball milling enhanced the insertion/extraction of Li-ions for CNTs.[20] These results suggest that structural defects caused by the chemical etching and mechanical treatment lead to more efficient intercalation/de-intercalation of Li-ions into the CNTs.[13] A binder-free CNT electrode has been widely investigated to increase the overall energy density in the battery system by removing the dead weight including an inactive polymeric binder and a conductive additive.[21, 22]

Graphene is a newly discovered carbon allotrope composed of a single atom layer of carbon. Recently, studies have further revealed many fascinating characteristics of graphene including ambipolar electric field effect,[23] quantum Hall effect at room temperature[24, 25] and high carrier mobility.[26, 27] The recent development of large-scale pattern growth of graphene films brings graphene closer to commercial reality. Graphene has also been investigated for use as an anode due to its exceptional electron transport, large surface area and excellent mechanical properties. Graphene has shown a considerably larger specific capacity than other carbon-based electrodes since Li can be stored on a variety of sites, including graphene edges, interlayer spaces between graphene layers, and both sides of the graphene surface. Yoo et al. reported the electrochemical characteristics of graphene with a specific capacity of 540 mAh/g, which can be improved to 730 mAh/g and 784 mAh/g by incorporating CNT and C_{60} into the graphene-based anodes, respectively.[28] The primary disadvantage of using graphene as an anode is the long Li-diffusion distance across the multiple layered graphene films with an extremely high aspect ratio, which requires Li-ions to overcome a high resistance. The slow Li-diffusion across the graphene layers was greatly improved by shortening the Li-diffusion distance via the artificial in-plane defects in the graphene sheets. [29]

Lithium alloy-based anode materials

Metallic/semi-metallic elements and various metal compounds can form Li-alloy in an organic electrolyte electrochemical cell.[30] A variety of metals such as Sn, Pb, and Bi and semi-metals such as Si, Ge, Sb, and As have been investigated for an anode material and have shown high lithium storage capacities.[31] Among these electrode materials, silicon has the highest known specific capacity of 3,579 mAh/g with a relatively low working potential.[32] One silicon atom can store up to 4.4 Li-ions corresponding to $Li_{22}Si_5$; however, the large volume changes during the charge/discharge cycles lead to rapid pulverization and degradation of the electrode material. The challenge is to retain silicon’s capacity after long charging/discharging cycles. Figure 1.2 shows typical behavior of Si electrodes; the capacity fades dramatically in the first few cycles due to the pulverization of Si materials and the loss of electrical contacts. Substantial efforts have been made to reduce the capacity degradation by using nanostructured silicon or silicon-based composites.

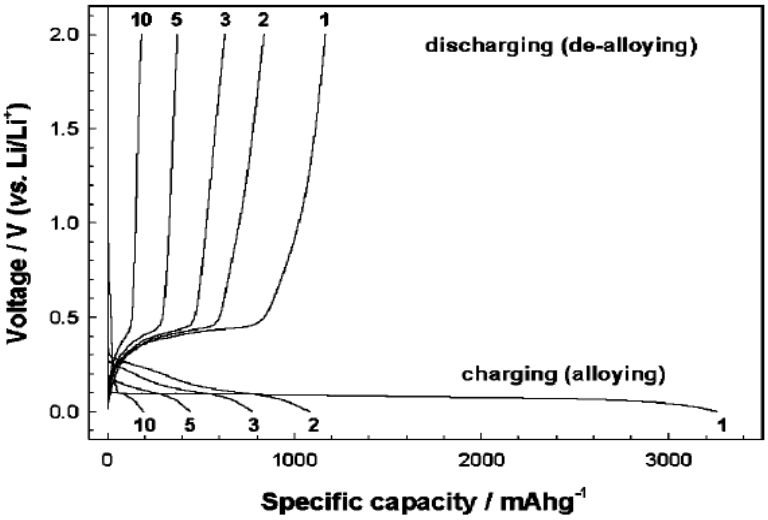

Figure 1.2 Galvanostatic charge-discharge profiles for 10 µm diameter-silicon powder anodes (active materials: Super P: PVDF=8:1:1 in weight, current density of 100 mAg^{-1}).[33]

When it comes to synthesizing nanostructured electrode materials, the size, shape, and dimensionality are the critical factors that affect the performance of LIBs. Nanostructured Si can be categorized into 0, 1, 2, and 3 dimensional materials, depending on the number of dimensions to define the nanostructure. The general solution to relieve significant volume changes is to produce 0-dimensional nanostructures such as silicon nanoparticles.[34, 35] Numerical simulation results suggested that Si nanoparticles under 150 nm in diameter can be cycled without fractures.[36] Although this approach alleviates some volume changes, experimental results show that the capacity fading still remains due to the agglomeration of Si nanoparticles.[37]

One-dimensional nanostructures such as Si nanowires[32] and nanotubes[38] provide a direct pathway for electron transport and enough void space to compensate for large volume changes. Cui et al. have grown a Si crystalline-amorphous core-shell structure of Si nanowires by a SiH_4 CVD method.[39] The crystalline core serves as a mechanical support and an efficient electrical conducting pathway while amorphous shells act as active sites to store Li-ions. In another interesting work, arrays of sealed Si nanotubes were fabricated with a sacrificial template for a precise control of morphology and void space in the electrode.[38] Two-dimensional nanostructures including nanofilms have shown excellent cycle stability over a large number of cycles.[40-42] Graetz et al. fabricated thin films of silicon anode using chemical vapor deposition methods with improved reversible lithium storage capability compared with conventional bulk silicon anode materials.[43] Takamura et al. demonstrated excellent cycle performance of 100 nm-thick Si film synthesized by a vacuum deposition method, exhibiting about a 2,000 mAh/g capacity even after 400 cycles, as shown in Figure 1.3.[41] The excellent cycle performance is attributed to the good adhesion of the Si film onto the dense metal substrate, as well as the excellent stress-resilient nature of the thin film. Last, three-dimensional nanostructures include the multilayer or bundles of 0- to 2-dimensional nanostructures[44] and porous bulk Si structures.[45, 46] Kim et al. reported the synthesis of 3D, porous bulk Si particles by thermal annealing of SiO_2 and butyl-capped Si particles.[45]

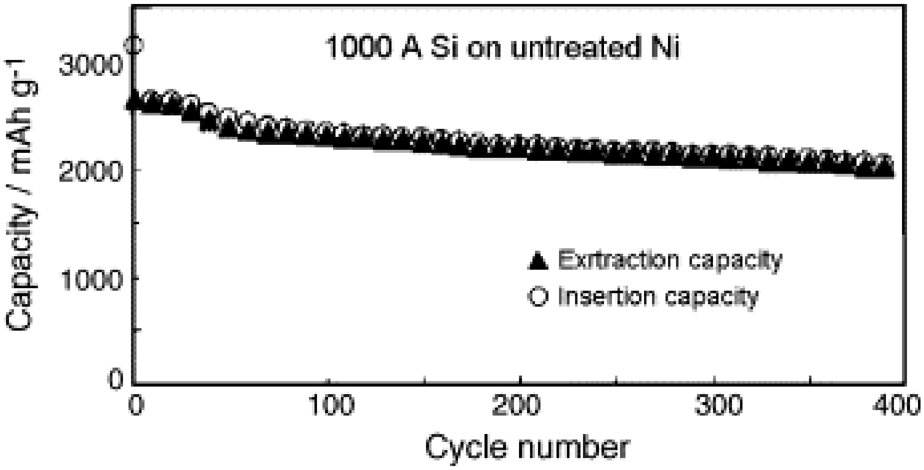

Figure 1.3 Cycle performance of 100 nm-thick Si films on Ni foil at the current rate of 1 C. [41]

The pore size of the bulk Si particles was about 200 nm with a wall thickness about 40 nm. This Si structure achieved a specific capacity of 2,800 mAh/g at a current rate of 2,000 mA/g over 100 cycles. The unique 3D, porous structure enabled the large specific capacity and faster Li-diffusion with an excellent cyclability.

Si/C hybrid anode materials

The limitations of Si-based electrode are attributed to the substantial volume change and poor electrical conductivity.[47] To effectively buffer the large volume changes of high capacity Li-storage materials, the active/inactive (or less active) supporting matrices are usually used to compensate for the volume changes. The supporting matrix should have good electrical conductivity and a strong structure for long cycle life. Carbon has been extensively used as the active supporting matrix due to its high electrical conductivity, good lithium storage capacity, small volume changes, low mass, compliance, and softness.[48]

One strategy for synthesizing the hybrid Si/C is to disperse the silicon nanoparticles in carbon matrices. Wang et al. synthesized hybrid structures of vertically-aligned carbon nanotubes (VACNTs) decorated with Si nanoparticles using a CVD method.[49] CNTs provided a strong mechanical support for the active materials and an excellent conducting channel for both electrons and Li-ions, while Si nanoparticles contribute to a high storage capacity of Li-ions. The solution-based spin-coating of Si/graphene films showed a good cycle performance by using the graphene to accommodate the large volume change of Si and to increase the electrical conductivity.[50] A multilayered Si nanoparticle (NP)/reduced graphene oxide (RGO) was synthesized by a simple dip technique, alternatively dipping in a Si NP and a RGO solution to construct layer-by-layer structures.[51] The free standing and flexible electrodes based on silicon NPs decorated on graphene oxide (GO) were synthesized by a vacuum filtration method.[52] A similar approach is to disperse the Si nanowires (NWs) into a GO matrix[53] and carbon cloth matrix[54] by a vacuum filtration and a spray coating, respectively, both demonstrating free-standing and flexible electrodes. The Si thin films have been investigated in a hybrid with carbon nanofiber[55] and carbon nanotube films[56, 57] to take advantage of the stress-resistant nature of Si thin films.

The different types of hybrid Si and nanostructured carbon, and their electrochemical performance are summarized in Table 1.2. The summary only includes binder- and conductive additive-free electrodes.

Table 1.2 Comparison of the electrical performance for different types of binder- and conductive additive-free hybrid Si/C electrodes.

Si Type	Carbon Type	Reversible capacity	Cycle number / Current rate	Si Synthesis methods	Reference
NP	VACNT	2,000 mAh/g	20 cycles / 100 mA/g	Silane CVD	[49]
NP	GO	1,611 mAh/g	200 cycles / 1,000 mA/g	Commercial	[50]
NP	GO	708 mAh/g	100 cycles / 50 mA/g	Commercial	[52]
NP	GO	765 mAh/g	300 cycles / 7200 mA/g	Commerical	[51]
NW	RGO	1,650 mAh/g	50 cycles / 840 mA/g	Silane CVD	[53]
NW	Carbon cloth	2,950 mAh/g	200 cycles / 840 mA/g	Silane CVD	[54]
Film	CNF	2000 mAh/g	30 cycles / 1250 mA/g	Silane CVD	[55]
Film	CNT film	500 mAh/g	150 cycles / 500 mA/g	Silane CVD	[56]
Film	CNT film	2,000 mAh/g	100 cycles / 1200 mA/g	Silane CVD	[57]

1.3. **Summary and conclusions**

The LIB has been widely used due to its high energy capacity. Graphite, the most commonly used anode materials, has shown excellent stability; however, the limited theoretical capacity cannot fulfill today's increasing demands for high power and energy capability for the next-generation batteries. In the past few decades, various materials have been studied to replace graphite electrodes, including nanostructured carbon (CNT and graphene) and lithium-metal alloys (Si).

Silicon is the most promising alternative to replace graphite electrode because it has the highest known theoretical specific capacity among all the elements. However, the challenge of using Si as an anode material is to accommodate the large volume change during lithiation/de-lithiation processes. Promising results have been produced with a Si thin film-based electrode, exhibiting stable cycle performance while maintaining high reversible capacity due to the stress-resilient nature of thin films. However, the loading amount of Si was insufficient to meet practical battery application requirements. One approach to increase the loading density of Si materials is to apply the Si films on a conductive matrix that has a large surface area. Carbon-based materials such as CNTs and graphene have been studied as the supporting matrix for active materials due to their high electrical conductivity, good lithium storage capacity, small volume changes, low mass, compliance, and softness.

1.4. Research objective and dissertation outline

The goal of my research is to develop new anode materials with improved energy density and high-rate charge/discharge capability while maintaining good cyclability, reliability, and safety. The new anode materials are based on Si films and substrate-bound nanostructures that are directly synthesized on current collectors without using a polymeric binder or other conductive additives. By eliminating the use of inactive materials, the total weight of the battery system decreases, resulting in a higher energy density. The substrate-bound electrodes also provide good electrical conductivity because of the small contact resistance between current collectors and active materials, ensuring an efficient electron transfer. We will introduce the fabrication processes of the hybrid materials and study the various factors on the design of electrode materials. The novel hybrid materials will be also systematically studied using various material characterization techniques and electrochemical tests.

This chapter, Chapter 1, presents an introduction and research objective of the study. The basic concepts of LIBs are introduced and a literature review on selective anode materials for LIBs is presented.

Chapter 2 contains the synthesis, characterization and electrochemical performance of a new graphene-based hybrid nanostructure. The highly branched graphene nanosheets are directly grown on a CVD-grown graphene film using a plasma-enhanced chemical vapor deposition method. The hybrids featuring unique morphology, high electrical conductivity, a large interfacial surface area, and high porosity are tested in an electrochemical cell.

Chapter 3 demonstrates the electrochemical performance of the hybrid Si film/highly branched graphene nanosheets. The Si films can be deposited on the highly branched graphene nanosheets using a low pressure chemical vapor deposition method that uses silane (SiH_4) as a precursor. The required void size for effective strain relaxation is investigated through simple theoretical calculations.

Chapter 4 introduces the fabrication of hybrid Si film/carbon nanofiber and its application for anode materials in LIBs. A synthesis method is described to grow carbon nanofibers on stainless steel without applying additional catalysts. A critical film thickness of Si to sustain the substantial volume change is calculated based on Griffith’s energy balance approach.

Chapter 5 covers the fabrication, characterization, and electrochemical properties of the hybrid carbon nanofiber/highly branched graphene nanosheets. The synergetic effect by integrating highly branched graphene nanosheets with carbon nanofibers on the electrochemical performance is investigated.

Chapter 6 presents the conclusion and summary of this dissertation and recommendations for future studies.

CHAPTER 2 STRAIGHTFORWARD FABRICATION OF A HIGHLY BRANCHED GRAPHENE NANOSHEET ARRAY FOR LI-ION BATTERY ANODE

2.1. Introduction

Li-ion battery (LIB) plays a dominant role in electrochemical energy storage. Their wide applications as power sources, from portable electronics to electric vehicles/hybrid electric vehicles, are mainly attributed to their superior energy density based on unit volume and unit weight over other battery systems.[58, 59] Growing demands for lighter, longer-lasting, and more powerful devices spur development of new electrode materials, because the performance of LIBs is highly dependent on the characteristics of electrodes. The ideal candidate for anode materials of LIBs should have high lithium storage capability and stable structure after repeated charge/discharge cycles.[32, 60, 61] Graphite is the most common anode material in LIBs since it was first commercialized by Sony Corporation in 1991, because of its abundance, high reversible energy capacity,[62] and electrochemical stability within a wide potential range.[63] However, current battery technology using graphite-based electrode is reaching its performance limit due to constraints by the theoretical specific capacity (372 mAh/g) of graphite.[64]

Significant effort has been made to develop novel anode materials based on carbon nanostructures to enhance electron transfer and kinetics.[65] Graphene, a newly discovered allotrope of carbon structure composed of a single atomic layer of carbon, is of special interest due to its exceptional electron transport,[23, 66] large surface area,[67] and excellent mechanical properties.[68] Ever since the discovery of electrochemical characteristics of graphene, researchers have actively investigated the use of graphene for energy storage systems. Graphene-based electrodes prepared by chemical routes such as Staudenmaier’s method[69] and Hummers method[70-72] and its composites[73, 74] have been extensively reported to improve capacity and cycle performance; however, there are still several intrinsic problems in thin film or expanded lamellar structure of graphene. One disadvantage is the long diffusion distance for the Li storage sites between graphene layers,[75] which are oriented perpendicular to the primary diffusion direction. Other major limitations include large irreversible capacity loss in the first cycle, poor stability in the subsequent cycles, and low electrical conductivity due to the high inter-sheet junction contact resistance.[76]

Another novel carbon nanostructure, namely carbon nanowalls (CNWs) or “vertically standing graphene sheets” discovered by Wu et al., can be described as a graphitic carbon nanostructure composed of a few layers of graphene vertically standing on a substrate.[77] Only a few studies have examined the electrochemical characteristics of CNWs. The first study on CNWs for anode materials in LIBs was conducted by Tanaike et al.[78] They reported the slurry method to prepare CNWs anode material because of its brittle structure. However, the conventional slurry method cannot fully take advantage of nanostructured CNWs by adding insulating polymer binder and inactive conductive additives.

Xiao et al. reported the CNWs synthesized via microwave plasma-enhanced chemical vapor deposition (MW-PECVD), enabling fast Li ion insertion/extraction performance because of its small domain size.[79] Recently, our group reported the CNW synthesis using direct current (dc) PECVD at atmospheric pressure.[80-82] This atmospheric method is capable of producing CNWs on various substrates (e.g., copper, silicon, stainless steel, carbon nanotubes) at a relatively low cost, thereby showing promise for large-scale applications. The resulting CNWs have shown to be attractive for room-temperature gas sensing,[80] discharge electrodes,[82] and transparent conductive electrodes.[83]

Herein, by further controlling the morphology and structure of the CNWs, we have synthesized highly branched graphene nanosheets (HBGNs) directly on a CVD-grown graphene film or underlayer on a Cu substrate. The direct growth of active materials on a current collector will promote stronger adhesion without losing electrical contact after long charge/discharge cycles. In addition, the hybrid graphene-HBGN nanostructure offers low intrinsic resistance at the electrode interface, significantly promoting the electron transfer. The fully grown CNWs form interconnected spherical granules consisting of HBGNs with a lateral dimension down to <5 nm. Different from two-dimensional graphene electrodes synthesized by wet-chemical routes, HBGNs with random orientation all over the substrate offer numerous diffusion paths for Li-ions. This method not only increases the specific mass capacity by removing inactive materials such as conductive additives and polymeric binders, but also enables the efficient electron and ionic transport through direct contacts between inter-connected graphene sheets and the substrate. Moreover, the unique morphology of three-dimensional HBGNs provides efficient diffusion of Li-ions with large surface area and many voids leading to a large number of sites for Li ion storage. This direct synthesis method under atmospheric pressure will create a new route to produce environmentally friendly, low-cost, and scalable HBGNs electrodes with high performance.

2.2. Experimental Method

Our electrode fabrication method is different from the traditional method of slurry mixing, coating and pressing, which potentially simplifies the electrode fabrication process in manufacturing. The electrode was fabricated by directly growing a graphene film and HBGNs onto Cu foil current collectors. Graphene films were grown on 25 µm-thick Cu foils using a CVD method[84] under atmospheric pressure. A Cu substrate of 1/2" in diameter was placed in 1" diameter quartz tube in a tube furnace and heated to 1,000 °C under H_2 and Ar flow. The annealing process was followed for 20 min to increase the Cu grain size, and a mixture of CH_4 and H_2 flow was introduced for 15 min to grow the graphene film. Lastly, the substrate was quickly cooled down to room temperature under the H_2 and Ar flow. HBGNs were subsequently synthesized on the graphene film without any catalysts using the PECVD process at atmospheric pressure as shown in Figure 2.1. The detailed description of the synthesis method can be found in previous reports.[80, 81, 85].

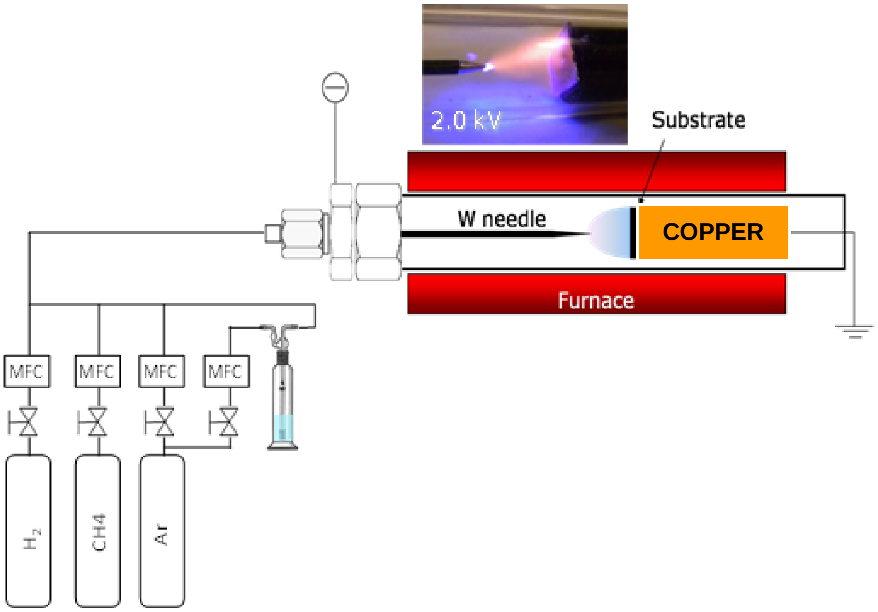

Figure 2.1 Experimental setup of plasma-enhanced chemical vapor deposition for HBGN growth.

In brief, HBGNs were fabricated in a tube furnace with a dc glow discharge between a tungsten tip and a copper foil substrate in a mixture of Ar/CH_4 at a flow rate ratio of 10 at 700 °C. All gas flows were controlled by GFC 17 mass flow controllers (Aalborg, Oraneburg, NY). The precursor gas of CH_4 (source of carbon), which flowed through a deionized water bubbler to provide the hydroxyl radicals, was introduced to the quartz tube in the furnace together with Ar. The temperature of the furnace was gradually increased to 700 °C with the Cu foil as a current collector placed on the grounded electrode to remove the copper oxide. Upon applying a high voltage between the tungsten tip and the copper foil, the Cu foil was coated with HBGNs under glow-discharge. After the growth, HBGNs were subsequently reduced thermally in H_2 flow at 900 °C for 2 h to remove O-containing functional groups. The electrode cooled down quickly to room temperature in the Ar atmosphere. The weight of the active materials (or HBGNs) was acquired by measuring the weight change before and after the HBGNs synthesis. A typical loading density of the active material is ~0.5 mg/cm^2. The growth time of HBGNs was about 1 h with a plasma power of 2.9 W.

The scanning electron microscopy (SEM) analysis was performed on a Hitachi S-4800 SEM with a stated resolution of 1.4 nm operated at 1 kV acceleration voltage. The transmission electron microscopy (TEM) analysis was conducted with a Hitachi H 9000 NAR TEM, which has a stated point resolution of 0.18 nm operated at 300 kV in the phase contrast, high-resolution TEM (HRTEM) imaging mode. Electrochemical measurements were conducted with 2032 type of coin cells. Lithium metal foil was used as the counter and reference electrode, and Celgard 2325 trilayer porous polymer membrane was used as the separator. The electrolyte was composed of 1M $LiPF_6$ solution in a carbonate mixture (EC:EMC=40:60 by volume). The cells were assembled in Ar-filled glove box with oxygen and moisture below 1 ppm. Electrochemical performance was evaluated at room temperature by the Maccor Series 4000 Battery Test System in galvanostatic mode and CHI650D electrochemical workstation.

2.3. **Results and Discussion**

The morphology and microstructure of the HBGNs were studied by scanning electron microscopy (SEM) and transmission electron microscopy (TEM), which clearly revealed that spherical granule-like HBGNs with 1-5 μm in diameter are uniformly formed on the surface of the substrate, as shown in Figure 2.2a. This surface-bound graphene network is expected to provide efficient electron transfer to the current collector, because all HBGNs branches are directly connected to the graphene film on the current collector (Figure 2.2b).

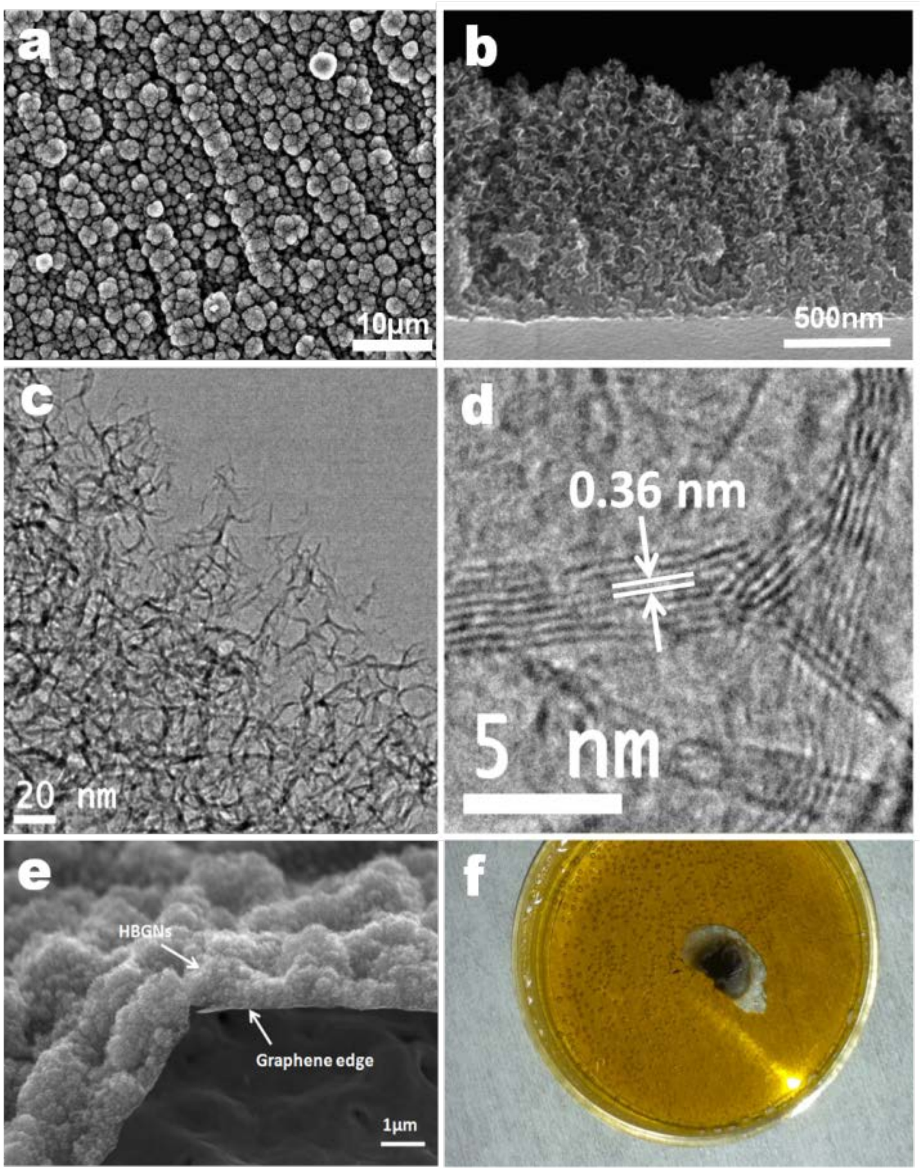

Figure 2.2 SEM image of top view (a) and side view (b) of HBGNs on a graphene film on a Cu foil; granule-like HBGNs are uniformly grown on the graphene film. TEM image (c) and HRTEM image (d) of HBGNs; highly dense graphene networks with small-sized graphene sheets. (e) Tilted SEM image of HBGNs on the graphene film; the bent edge of graphene film that was peeled off from the substrate clearly shows the deposition of HBGNs on the graphene film. (f) HBGNs on the graphene film after etching Cu foil

using 1M $FeCl_3$ + 1M HCl; the bright side of the rim is the graphene film without deposition of HBGNs.

Raman spectroscopy study of graphene films indicates the existence of multi-layer graphene films (Figure 2.3). The hybrid graphene-HBGN structure features low intrinsic resistance between the HBGNs and the graphene film. The graphene nanosheets grown in the final stage were extremely small with lateral dimension down to <5 nm (Figure 2.2c). This unique morphology offers plenty of lithium storage sites, including: i) micro/nano cavities; ii) graphene surface and edges of graphene; and iii) the interspace between graphene layers. HRTEM images of HBGNs (directly deposited on a copper TEM grid) show that the number of graphene layers is 8 and the interplanar spacing is 0.36 nm (Figure 2.2d), which is larger than that of conventional graphite (0.34 nm) due to the presence of oxygen-containing functional groups [80].

The as-grown CNWs contain significant amount of oxygen-containing groups and can be greatly reduced after 900 °C treatment in H_2 for 2 h. The copper substrate from the electrode can be removed by an acid etching without breaking its structure (Figure 2.2e, f), indicating a highly stable hybrid nanostructure of graphene-CNWs, which holds great potential as a free-standing LIB electrode (Figure 2.4).

Figure 2.5 shows the SEM images of the intermediate products during the HBGNs growth process. In the early stage (Figure 2.5a), dissociated carbon precursors under glow-discharge plasma nucleated on the grounded surface and grew into vertically-oriented graphene on the substrate with lateral width of ~200 nm as shown in Figure 2.5b.

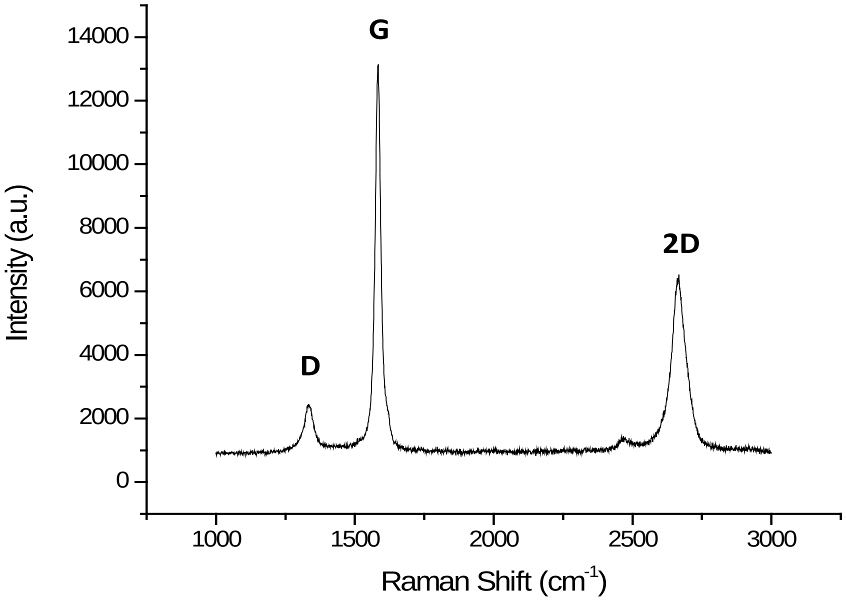

Figure 2.3 Raman spectrum of CVD-grown graphene on a copper substrate. The graphene film was transferred to a Si wafer for Raman spectroscopy measurements.

Then, more graphene sheets nucleated on the open edges and some were found on the surface of pre-existing graphene sheets. It should be noted that the domain size of the graphene sheets became smaller as the growth evolved (Figure 2.5c). In the final stage, HBGNs were self-assembled and formed spherical granules (Figure 2.5d). The HGBNs have a high surface area of 269 m^2/g, as measured by the N_2 adsorption Brunauer-Emmett-Teller (BET) method (Figure 2.6).

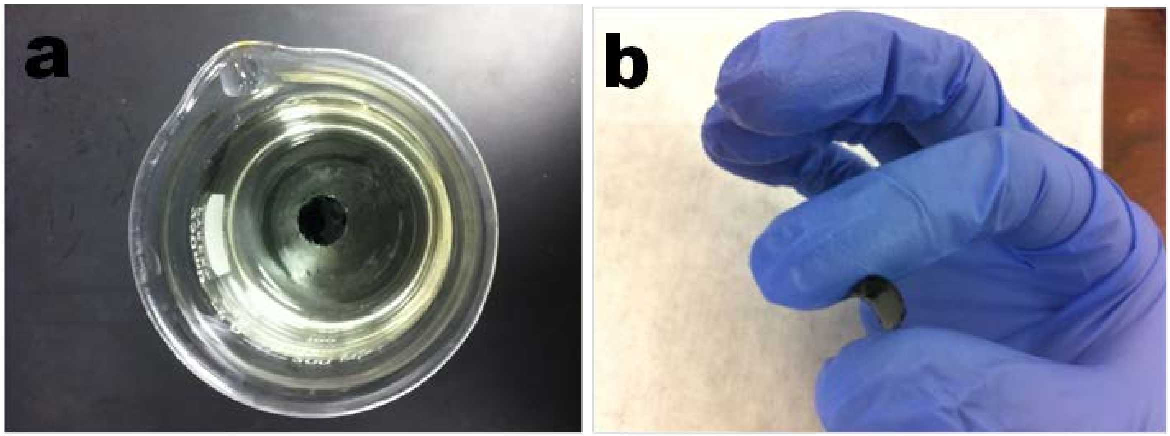

Figure 2.4 HBGNs with a graphene underlayer on Polydimethylsiloxane (PDMS) are floating after etching Cu foil using 1M FeCl3 + 1M HCl (a) and the flexible HBGNs/graphene/PDMS composite (b).

The electrochemical performance of the HBGNs electrode was characterized by galvanostatic cycling at a current density of 50 mA/g with a voltage ranging from 0.01 to 2.0 V vs. Li^+/Li, as shown in Figure 2.7a. HBGNs with the graphene film showed capacity of as high as 461 mAh/g after 100 cycles, which is much higher than that of the theoretical specific capacity of graphite (372 mAh/g; corresponding to a stoichiometry of

LiC_6). In contrast, electrodes without the CVD-grown graphene film, i.e., HBGNs-only electrodes, exhibited very poor cycle stability, losing 25% of reversible capacity after only 30 cycles, as shown in Figure 2.7b.

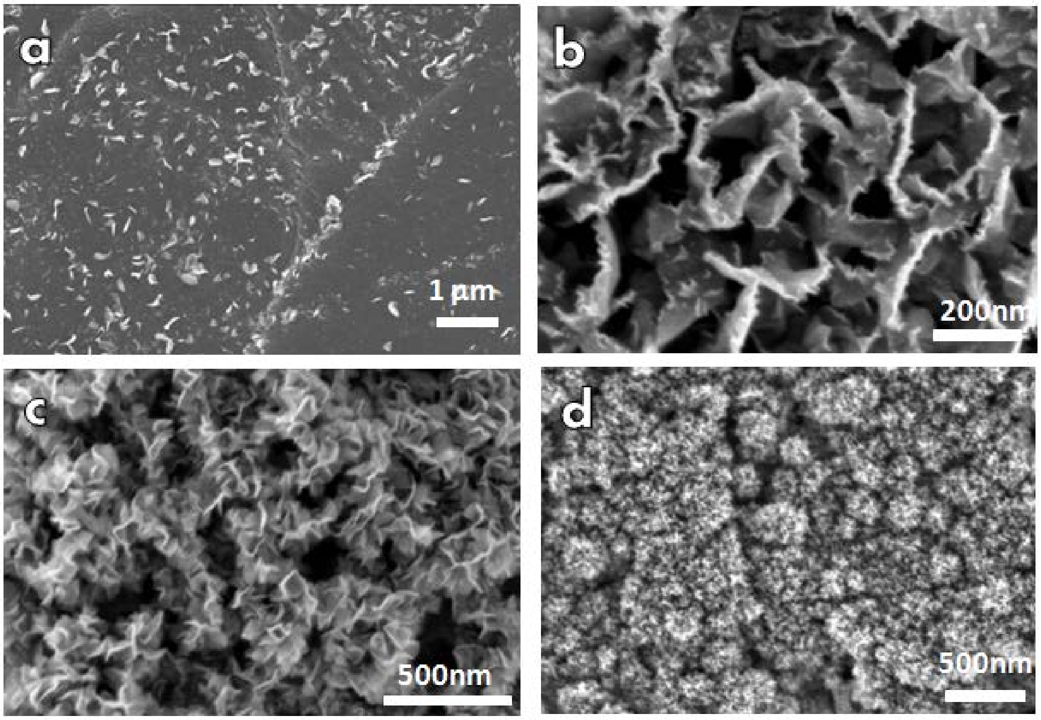

Figure 2.5 Growth stage of HBGNs on the graphene film at different growth time: 1min (a), 5 min (b), 10 min (c), and 30 min (d). New graphene sheets with smaller domain size nucleate on the surface and edge of existing graphene sheets.

Excess lithium storage on highly branched and disordered carbon nanostructures may be attributed to the unique structure and morphology of HBGNs characterized by micro/nano cavities,[86] turbostratic structure (or disordered stacking of graphenes with random rotations or translations),[87] and edges of standing graphene nanosheets. However, irreversible capacity loss in the first cycle is more than 50%, as generally observed for graphene-based electrodes. This loss may be attributed to the reductive decomposition of the electrolyte and the formation of solid electrolyte interface (SEI) film due to large surface area and irreversible reaction of Li-ions with the residual oxygen-containing functional group of the HBGNs.[88]

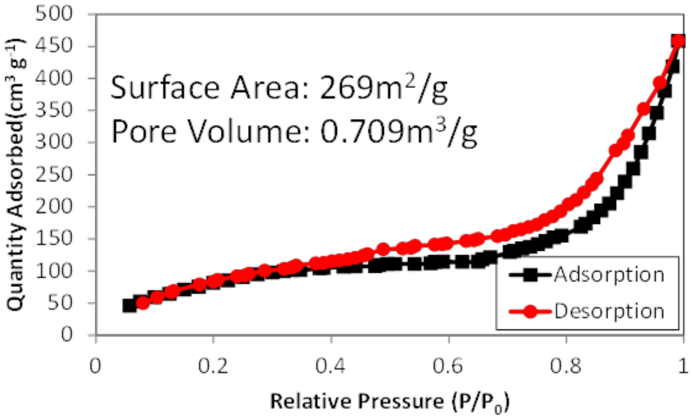

Figure 2.6 Adsorption/desorption curve of HBGNs.

The profiles of galvanostatic charge/discharge curves of HBGNs show a similar pattern to graphene-based electrodes (Figure 2.7c), suggesting that the Li storage mechanism of HBGNs is comparable to that of the graphene-based electrode prepared by wet-chemical synthesis. It was reported that disordered stacking of graphene layers provided nonequivalent Li ion sites; no distinct plateau was formed as observed in graphite electrodes.[70]

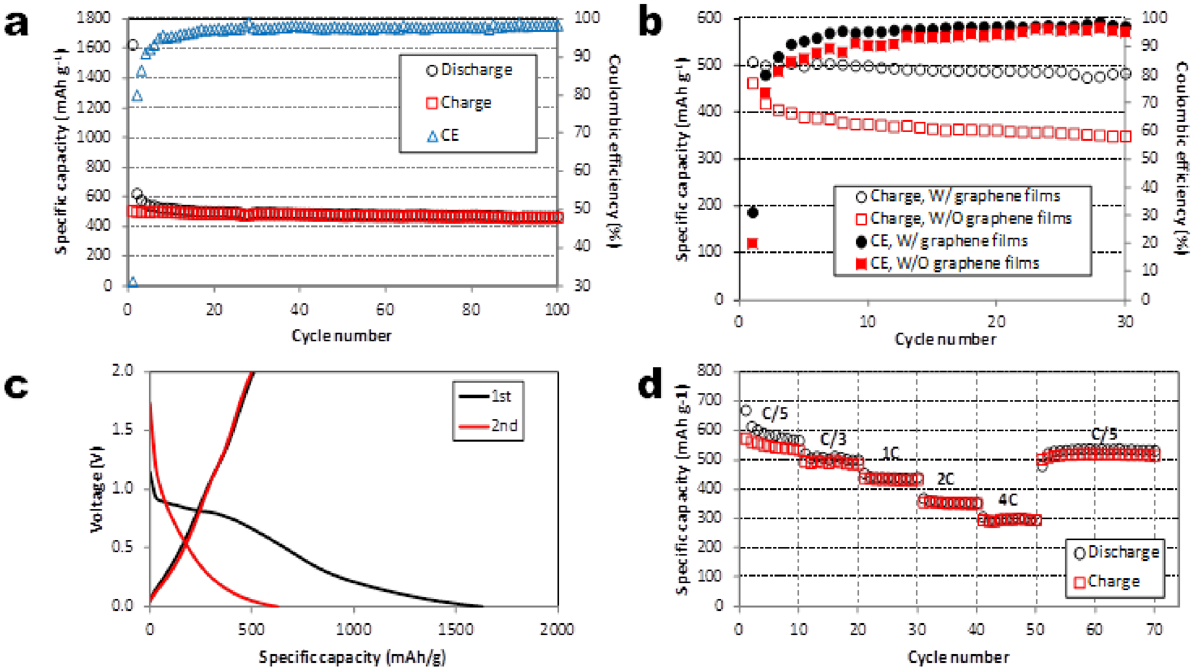

Figure 2.7 Electrochemical performance of HBGN electrodes. (a) Cycle performance (charge, discharge, and Coulombic efficiency or CE) between 0.01 and 2.0 V at a rate of C/5 (current density of 50 mA/g) for HBGNs with a graphene underlayer. (b) Comparison of the cycle performance of the HBGN electrode with and without the underlying graphene film. (c) Galvanostatic charge/discharge cycle at a current rate of C/5 in the first two cycles. (d) Rate performance of HBGNs on the graphene film at various current densities; the coin cell was cycled at C/26 in the first 3 cycles and subsequently cycled at higher current rates.

In the first cycle, a plateau around 0.8 V is likely caused by the SEI layer formation, which was not observed in the second cycle. After the first plateau, the voltage rapidly decreased and the second plateau occurred at ~0.2 V. Li-ion intercalation into thegraphene layers (defined as discharging in this study) is responsible for the capacity of the potential region lower than 0.5 V (vs. Li/Li+). The capacity above 0.5 V may be attributed to the mico-cavities formed between extremely dense graphene sheets and the Faradic capacitance on the surface or on the open edges of graphene sheets.[89] HBGNs are composed of ultra-small domains with open edges of graphene sheets, resulting in effective diffusion of Li-ions, and hence good rate performance. We investigated the rate performance of HBGNs at various current densities in every 10 cycles, as shown in Figure 2.7d. The charge/discharge cycles started with a low current rate of C/26 in the first 3 cycles, and the rates were increased gradually. The reversible capacities were obtained as 550 mAh/g at C/5, 493 mAh/g at C/3, 434 mAh/g at 1C, 354 mAh/g at 2C, and 297 mAh/g at 4C, which can be explained by the increasing resistance at the interface between the electrolyte and the active materials at a higher current rate. A reversible capacity of 518 mAh/g was obtained after lowering the current density back to C/5, which indicates excellent cycle stability.

The HBGNs electrodes reported here have many advantages compared with previously-reported vertically-aligned graphene electrodes or CNWs. Tanaike et al.

reported a conventional slurry-coated CNWs electrode, having a reversible capacity of 250 mAh/g at a current density of 100 mAh/g.[78] Xiao et al. investigated the electrochemical characteristics of as-grown CNWs on nickel substrates as negative electrodes and obtained a reversible capacity of 380 mAh/g at C/3 and 280 mAh/g at C/0.375.[79] The electrochemical performance of HBGNs electrodes was significantly enhanced in terms of specific capacity and charge/discharge rate due to the strong adhesion of hybrid materials on the current collector and the nanosized graphene domain.

The Nyquist plot was used to understand the better electrochemical performance of the HBGNs electrode with graphene underlayer, compared to that without graphene underlayer. As shown in Figure 2.8, the Nyquist plots of the HBGNs electrodes, measured at the discharge potential of 1.47 vs. Li/Li^+ after two cycles, consist of a semicircle at the high frequency zone and an inclined line at the low frequency region, representing charge transfer and Li-ion diffusion processes, respectively.[90] The HBGNs electrode with graphene underlayer exhibits a smaller diameter, suggesting a smaller charge transfer resistance.

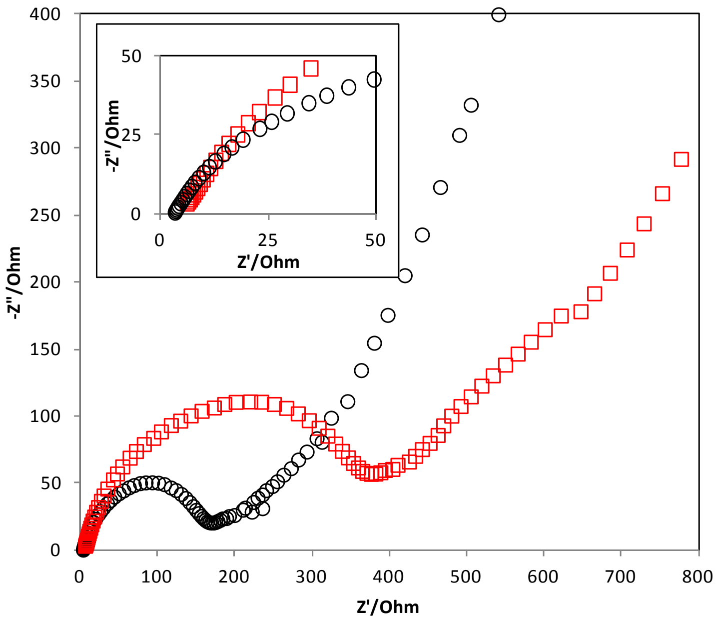

Figure 2.8 Nyquist plot of HBGNs with a CVD-grown graphene film between the current collector and HBGNs (circle) and HBGNs without the graphene film on the current collector (square). The inset is an enlarged plot showing the intercept on Z' axis.

Meanwhile, from the intercept on the Z' axis at high frequency region as shown in Figure 2.8 inset, the ohmic resistances of the cells with and without graphene underlayer are 3.1 and 4.9 Ohm, respectively. This possibly resulted from the fact that the HBGNs electrode with a graphene underlayer possesses a better electrical contact between the current collector and HBGNs because the values of the ohmic contribution from the electrolyte and separator in the both cases could be considered to be same. These results are in good agreement with the fact that the HBGNs electrode with graphene underlayer possesses better electrochemical performance.

2.4. **Conclusions**

HBGNs directly grown on a CVD-grown graphene film using dc PECVD under atmospheric pressure delivered promising electrochemical performance due to highly conductive nano-sized graphene sheet networks with features of high density, large surface area, and high porosity. The hybrid graphene-HBGN structure was successfully designed to maintain its integral structure after long cycles. A specific capacity of 500 mAh/g at a current density of C/5 was obtained with 10% irreversible capacity loss after 100 cycles. The HBGNs electrode retained good specific capacity of 297 mAh/g even at a high rate of 4C. The synthetic procedure of the additive-free HBGNs electrode is fairly simple, energy-efficient, and applicable for any conductive substrates, promising for large-scale applications.

Due to their unique morphology and structure, HBGNs have great potential as supporting matrices in composite materials for LIB anodes. A thin film of Si will be deposited on the large surface of HBGNs using low pressure CVD (LPCVD) from silane (SiH_4). The combination of Si thin films and HBGNs is expected to deliver excellent electrochemical performance.

CHAPTER 3 NOVEL HYBRID SI FILM/HIGHLY BRANCED GRAPHENE NANOSHEET AS AN ANODE MATERIAL FOR LITHIUM-ION BATTERIES

3.1. **Introduction**

Tremendous efforts have been made to further improve energy density, cycle performance and high-rate capability of lithium-ion batteries (LIBs) that are required for high-power and high-energy applications such as power tools and electric vehicles. Silicon as the anode material in LIBs has the highest theoretical specific capacity of 3,579 mAh/g, which is over ten times higher than that of commercial carbon-based anodes.[31] Despite the excellent lithium storage capability of Si, a big challenge remains to overcome the pulverization and rapid capacity fade of Si electrodes due to the large volume expansion up to 300% during Li alloy/de-alloying with Si, which is the main obstacle to commercialize Si electrodes.

Over the past few years, considerable research has explored the Si-based electrodes for anode materials in LIBs. With substantial progress in nanotechnology, nanostructured Si has been widely studied and has shown several advantages over bulk Si materials, including effective strain accommodation and a short lithium diffusion path.[38, 47, 91] Recent studies on nanostructured Si anode have shown promising electrochemical results.[91-93] Another strategy to resolve the issue is to design hybrid materials that consist of Si and different types of carbon structure such as carbon nanotubes,[56, 57, 94] carbon nanofibers,[57, 95] and graphene[29, 96, 97] to host Si nanomaterials. Nanostructured carbon as the host matrix provides an efficient pathway for Li-ion, a robust supporting structure, efficient electron transfer, and a large surface area. Previously our group reported that a highly branched graphene nanosheet (HBGN) has shown promising electrochemical performance as an anode material in LIBs.[98] The specific capacity of HBGN was 500 mAh/g at the current rate of C/5 (or 50 mA/g) with stable cycle stability. The rate performance of HBGN was also found to be excellent with a specific capacity of 297 mAh/g at 4 C.

In this study, we designed a novel hybrid Si/HBGN and explored the possibility of the synergetic effect of the hybrid for high lithium storage capability. HBGNs, several layers of graphene sheets that are vertically oriented to the substrates, have been synthesized via a direct current plasma-enhanced chemical vapor deposition (PECVD) method at atmospheric pressure. The conductive network of HBGNs serves as the host matrix for Si films with a large surface area and a mechanical supporting structure. The direct deposition of HBGNs on current collectors makes the electrode fabrication process simple and economical, but the process also removes the dead weight by obviating inactive additives such as conducting carbon and polymeric binders. Low pressure CVD

(LPCVD) using silane gas (SiH_4) has been used to apply amorphous Si film conformally to the highly porous HBGN substrate.

In comparison with the two-dimensional layer structure such as graphene paper produced by the solution-based processes, HBGNs offer better accessibility for the Si deposition, thus promoting rapid access of Li-ions into the Si films. The size effect of void space on the large volume change of Si was explored by controlling the thickness of Si films on a limited void space in the HBGN substrate. While many studies have been done on the hybrid Si nanoparticle/graphene as anode material,[29, 52, 96, 99, 100] there is only one report by Evanoff et al., to our knowledge, on the hybrid Si film/graphene.[74] The main difficulty in synthesizing the hybrid lies in the conformal coating of Si films on a two-dimensional graphene structure. The binder-free and three-dimensional HBGNs can resolve the issue. The electrochemical performance of Si/HBGN is also comparable with those obtained by Evanoff et al. with Si coated graphene granules, which were made by slurry-coating with chemically reduced graphene oxide and LPCVD for Si. Last, we investigated the minimum void space to allow the volume expansion of Si.

3.2. **Experimental method**

The Si/HBGN growth consists of two steps: dc-PECVD for HBGN synthesis and LPCVD for Si film deposition. The detailed synthesis of HBGN can be found in Chapter 2. In short, the dc-PECVD was conducted to grow HBGNs on the stainless steel substrate

(25 µm, Alfa Aesar) that also served as the current collector. The half-inch in diameter stainless steel substrate was placed on a grounded copper rod and put into a quartz tube furnace. The temperature of the furnace was kept at 700 °C during the synthesis process. The CH_4 as the carbon source and Ar as the carrier gas with a 1:10 flow ratio were introduced into the reactor with water vapor. High voltage with a plasma power of 2.9 W was applied to generate a dc glow discharge between two electrodes. The pin-plate electrodes generated a highly focused electric field, and dissociated methane gas molecules in high temperature were nucleated on the surface of the current collector. The electric field that formed vertically to the substrate directed the growth direction of the graphene nanosheets. The newly formed graphene domain size became smaller as the synthesis progressed. After a certain period of growth, the plasma and CH_4 flow were turned off. Subsequently, the temperature of the furnace was increased to 900 °C and the sample was thermally annealed under a hydrogen atmosphere to reduce the oxygen functional group on the as-produced graphene nanosheets. The HBGNs were put into an LPCVD reactor for Si film deposition. The reactor was purged with high purity Ar and vacuumed under 30 Torr. When the temperature of the furnace reached at 500 °C, the SiH_4 flow was introduced into the reactor. The heated SiH_4 gas was decomposed and started to form Si film on the surface of the HBGN in the reactor.

$$SiH_4\,(g) \rightarrow Si\,(s) + 2H_2\,(g)$$

Subsequently, carbon coating was conducted at 600 °C with a C_2H_2 precursor gas.

The Si/HBGN on stainless steel was transferred to the glove box to be used as an anode and assembled in a type 2032 coin cell for electrochemical tests. The coin cell consisted of lithium metal as the counter- and reference electrode, Celgard 2325 trilayer porous polymer membrane as the separator, electrolyte (1M $LiPF_6$ solution in a carbonate mixture EC:EMC=40:60 by volume), and a Si/HBGN electrode. All assembly procedures were conducted in an Ar-filled glove box oxygen and a moisture level below 1 ppm. Scanning electron microscopy (SEM) analysis was performed on a Hitachi S-4800 SEM with a stated resolution of 1.4 nm operated at 1 kV acceleration voltage. Transmission electron microscopy (TEM) analysis was conducted on a Hitachi H 9000 NAR TEM, which has a stated point resolution of 0.18 nm operated at 300 kV in the phase contrast, high-resolution TEM (HRTEM) imaging mode.

3.3. **Results and discussion**

The hybrid Si/HBGN electrode was prepared via a two-step CVD method. The HBGN served as a supporting structure composed of vertically-oriented graphene sheets with a large surface area and good electronic conductivity. Subsequently, Si film was coated on the HBGN surface as active sites for Li-ion storage.

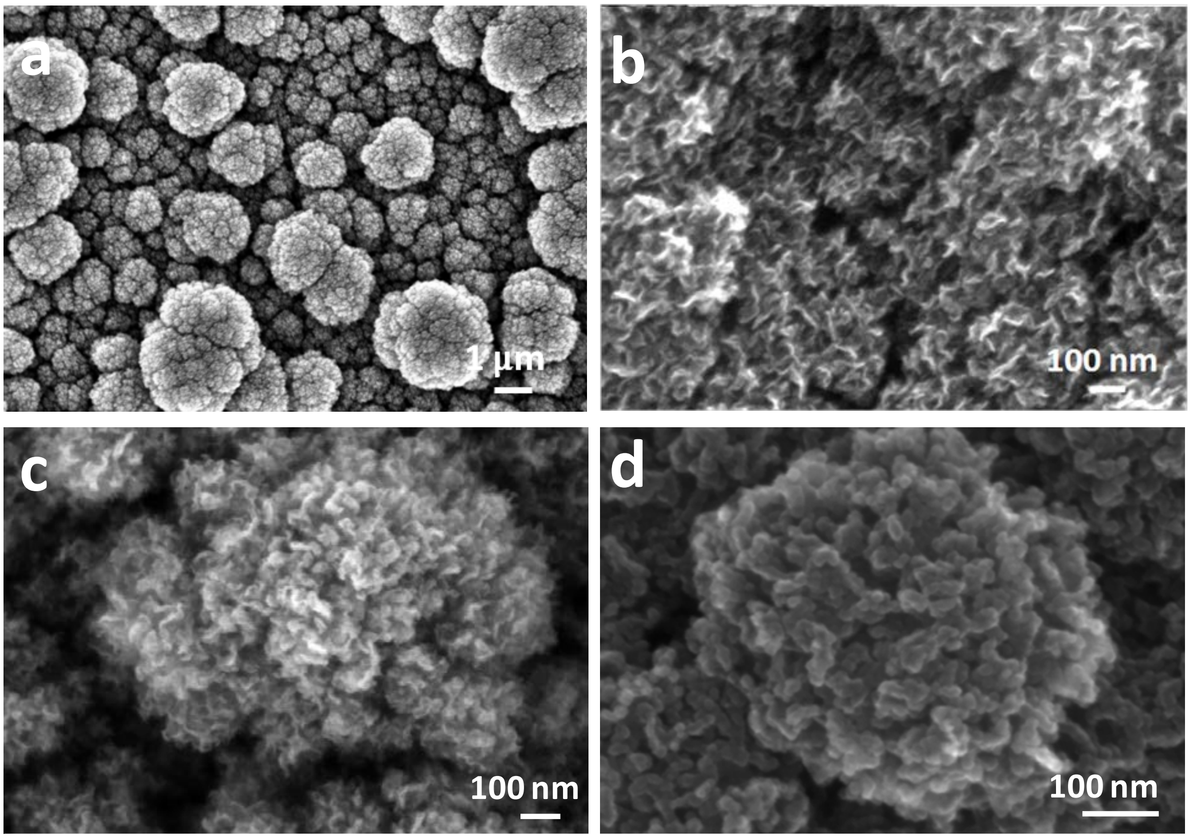

Figure 3.1 (a) and (b) SEM images of HBGNs before Si deposition. (c) Sample A: HBGNs after 0.5 hr Si deposition. (d) Sample B: HBGNs after 1 hr Si deposition.

In Figure 3.1a and b, the SEM image of the pristine HBGNs shows the vertically-oriented graphene sheets. This structure contains distinct interspace voids between the graphene sheets. The graphene nucleated on the surface and the edges of pre-existing graphene nanosheets, and eventually the HBGNs grew denser as the growth time increased. As a result, the void space became smaller. The growth time of HBGNs was maintained under 10 min to ensure enough void space in the three-dimensional HBGN structure. Figure 3.1c clearly shows that the thickness of the graphene nanosheets of the HBGNs was increased after the Si deposition and the void space between the graphene nanosheets became smaller. However, the configuration of the HBGNs still maintained its structure even after the Si deposition. With increased Si growth time in the LPCVD process, the Si/HBGN exhibited a much smaller void space, as shown in Figure 3.1d. Energy dispersive X-ray spectroscopy (EDS) analysis was conducted to examine the Si film on the HBGNs.

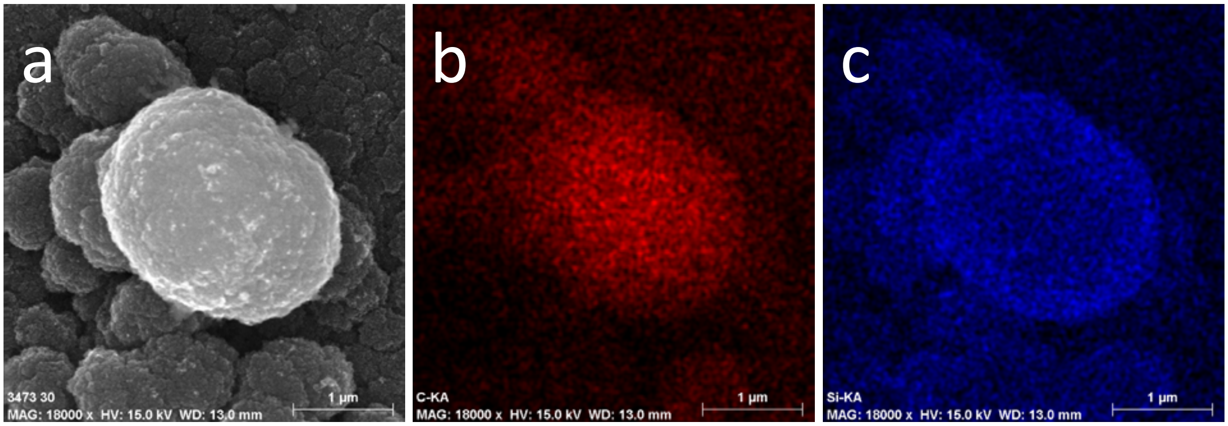

Figure 3.2 EDS elemental maps of Si/HBGN (a) SEM secondary electron image, (b) Carbon map, and (c) Silicon map

Figure 3.2 shows that EDS elemental maps of silicon and carbon on the hybrid materials clearly indicate that Si films are uniformly deposited on the surface of the HBGNs. The as-produced Si/HBGN on a stainless steel substrate was assembled in a half-coin cell for electrochemical tests. In this study we defined the charging and discharge processes as de-lithiation and lithiation of Si, respectively. In Figure 3.3a, the electrochemical tests show that the Si/HBGN reached a highest discharge capacity of 1,740 mAh/g with good cycle life. The galvanostatic cycling at the current rate of 1 C (or 2,000 mA/g) was used with a cutoff potential between 0.01-2.0 V for the test. There was a slight increase in specific capacity up to 45 cycles due to the increased Si activation and the specific capacity gradually decreased as the cycles increased. The capacity loss may be ascribed to the unstable SEI layer formation, which increases the diffusion resistance and consumption of a large amount of Li-ions during cycling. The reversible specific capacity retained 1,000 mAh/g at the 120th cycle. The Coulombic efficiency for the first cycle was 63 % and increased over 97 % for the rest of the cycles. The irreversible capacity loss in the first cycle is mainly attributed to the SEI formation. Figure 3.3b shows typical voltage profiles of charge/discharge curves of Si/HBGN. There was a sharp drop in the voltage to about 0.1 V and a long plateau at 0.1-0.01 V forming an amorphous Li_xSi phase.

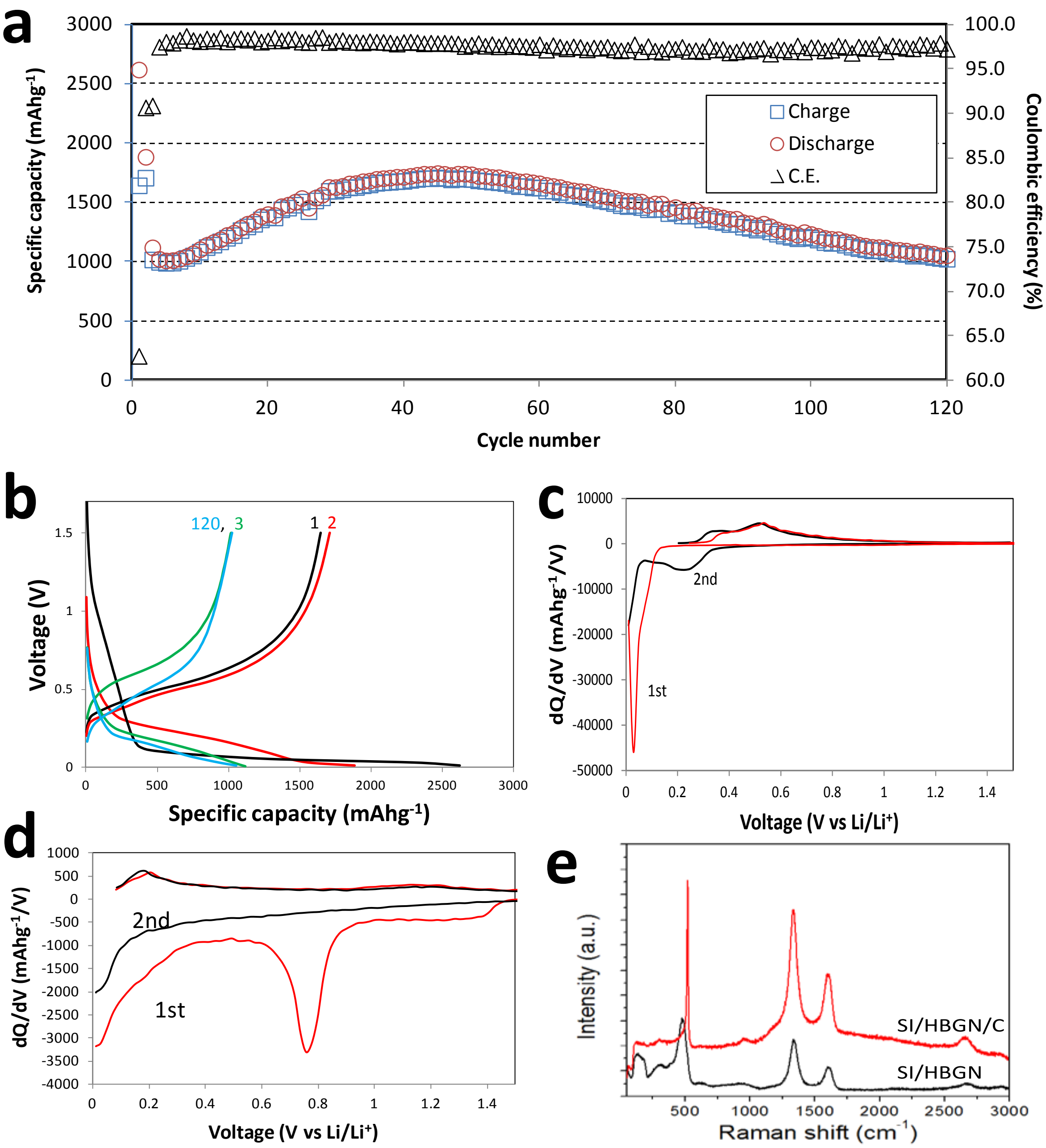

Figure 3.3 (a) Cycle performance (charge, discharge, and Coulombic efficiency or CE) of Si/HBGN electrode between 0.01 and 1.5 V at a current rate of 0.05 C (or 100 mA/g) in the first 2 cycles, and 1 C (or 2000 mA/g) for the rest of the cycles. (b) Voltage profiles of Si/HBGN electrode. (c) Differential profiles of Si/HBGN during first 2 cycles. (d)

Differential profiles of HBGN during first 2 cycles. (e) Raman spectroscopy of Si/HBGN before and after carbon coating (red line: Si/HBGN/C, black line: Si/HBGN)

No other plateau that corresponded to the Li intercalation into the HBGNs was observed. The reversible capacities of the third and the 120th cycle were both close to 1,000 mAh/g, but the voltage profile after the 120th cycle was slightly lower than that of the third cycle. The dQ/dV profiles of Si/HBGN are shown in Figure 3.3c. The differential capacity (dQ/dV) was acquired by numerical differentiation of the galvanostatic cycling data. There was sharp anodic peak at 0.03 V in the first discharge curve, which is attributed to the coexistence of two phase region of amorphous Li_xSi and crystalline Si. A broad peak at 0.24 V was observed in the second discharge curve suggesting the formation of amorphous Li_xSi. In the charging curve, the peaks at around 0.3 V and 0.5 V were related to the Li de-alloying reaction forming amorphous Si.

On the other hand, dQ/dV profiles of HBGN in Figure 3.3d showed a peak at around 0.8 V that was ascribed by the SEI formation and the peak disappeared in the second discharge curve. The large amount of lithium was consumed during the SEI formation due to the large surface area and the remaining oxygen-containing functional group, which resulted in a huge irreversible capacity in the first cycle. After synthesizing the Si/HBGN, a thin layer of carbon was deposited on the hybrid using the CVD method to

(1) stabilize the solid electrolyte interphase (SEI) formation, (2) improve the electrical conductivity and (3) help to buffer the volume change.[45, 103, 104] Figure 3.3e shows Raman spectra of Si/HBGN with and without a carbon coating. The Raman spectrum contains the characteristic D and G bands around 1,360 and 1,590 cm^{-1}, respectively, typical for graphitic carbon. A broad peak at 476 cm^{-1} and two broad humps at 100-200 cm^{-1} and 200-300 cm^{-1} are typical characteristics of amorphous silicon. These peaks disappeared during the carbon coating process at 600°C and a sharp peak appeared at 519 cm^{-1}, corresponding to the crystalline phase of Si. The exposure to a high temperature during the carbon coating resulted in the crystallization of the amorphous Si film.

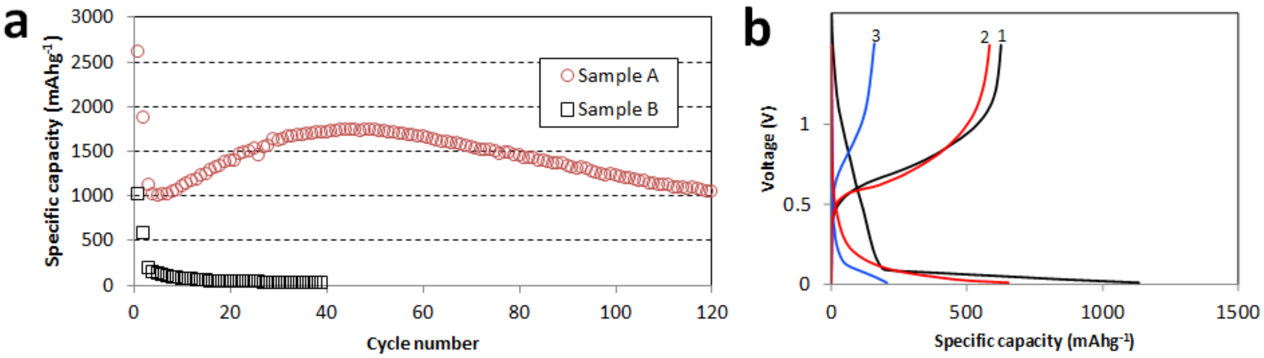

Figure 3.4 (a) Comparison of the cycle performance of an HBGN electrode with different Si coating thicknesses (current density in the first 2 cycle at C/20, the rest at 1 C). (b) Voltage profiles of HBGN with a 25 nm-thick Si film.

To investigate the effect of void space in the Si/HBGN on the electrochemical performance, an HBGN electrode with a thick deposition of Si film (sample B) was prepared. The deposition amount of Si was increased with the growth time. Accordingly, the sample B had a small void space and the individual branch-like graphene sheets could not be observed (Figure 3.1d). The Si loading density of the sample B was 0.07 mg/cm^2, which is about twice higher than that of sample A, as shown in Table 3.1. The growth condition for samples A and B were the same except for the SiH_4 growth time.

The electrochemical test was performed using sample B. Figure 3.4a compares the cyclic performance on the two samples. The reversible capacity of the thick Si/HBGN (sample B) dropped dramatically within a few cycles, indicating that the Si films failed to accommodate the high mechanical stress and led to pulverization. Figure 3.4b shows the charge/discharge profiles of sample A and sample B in the first cycle. Although the detailed failure mechanisms are not clear for sample B, we expect that the confined Si film with a limited void space could not release the strain effectively. At the same time, the HBGNs did not provide enough mechanical robustness to prevent the loss of electrical contact. To realize the excellent cycling performance of the Si/HBGN electrode, there was a very limited loading amount of Si film on HBGNs because of the small void space in the HBGN. The thickness of Si film can be decreased by reducing the LPCVD growth time and lowering the SiH_4 flow rate. Interestingly, we only were able to observe a thin layer of Si deposition even in the short duration of synthesis, which is different from the Si nanoparticles' deposition using LPCVD with SiH_4 by the Kumnta group. [94]

Table 3.1 Comparison of Sample A and B with different growth conditions.

	Si Loading density (mg/cm^2)	SiH_4 flow rate (sccm)	Growth time (hr)	Average t (nm)	Required void spacing d (nm)
Sample A	0.03	50	0.5	14	104
Sample B	0.07	50	1.0	25	185

The critical fracture stress increases as the thickness of the Si film decreases, as described in the Griffith-Irwin criterion:

$$\sigma_{fracture} = K/\sqrt{\pi h} \quad \text{Eq. (3.1)}$$

where $\sigma_{fracture}$ is the critical fracture stress, K is the fracture toughness and h is the film thickness. However, a large loading density is needed to increase the overall energy density of the battery system. Therefore, it is important to design the Si-based electrode within an allowable loading amount to provide enough void space for stable battery performance. When Si reacts with lithium to form $Li_{3.75}Si$ at room temperature, the volume of the Si is expanded about 270 %.

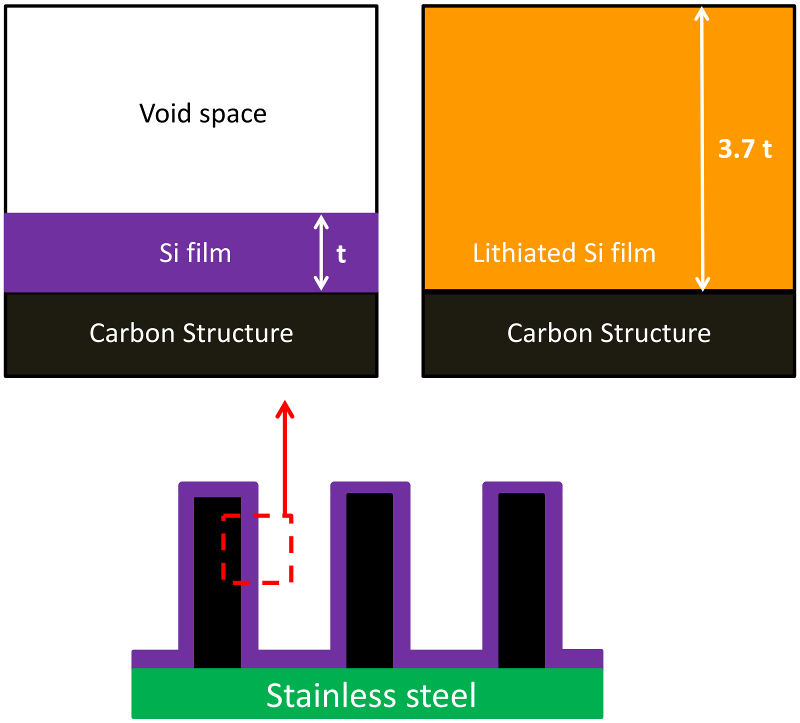

Figure 3.5 Idealized geometry of Si film on carbon structure from the cross-sectional view before/after Si lithiation.

To understand how much void space is necessary for the volume expansion, we calculated the theoretical volume expansion percentage of Si.[105]

$$\frac{V_f - V_i}{V_i} \times 100 = \Delta V\ (\%) \qquad \text{Eq. (3.2)}$$

$$V_f = 3.7V_i \qquad \text{Eq. (3.3)}$$

where V_f is the final volume, V_i is the initial volume and ΔV is the percentage of change of the volume expansion in Si materials. Considering the full Si lithiation for simplicity, the final volume of Si will be expanded 3.7 times the original volume of Si. Using this relation, we can estimate the required void space for Si to compensate for the volume expansion during lithiation/de-lithiation. Si film is bonded on the surface of graphene sheets and constrained from expanding by them. Therefore, the Si film is only allowed to expand perpendicular to graphene surface or expands anisotropically, which may increase the thickness of the film up to 3.7 times larger than the original thickness. To avoid the interference between adjacent Si films, the minimum required void spacing (d) should be 7.4 times larger than the film thickness (t).

$$d > 7.4\,t \qquad \text{Eq. (3.4)}$$

The average film thickness of Si can be estimated as shown in the following equation by dividing the mass per unit area by the density of Si film.

$$t = \frac{1}{BET} \times \frac{M_{Si}}{M_{HBGN}} \times \frac{1}{\rho_{Si}} \qquad \text{Eq. (3.5)}$$

where BET is the Brunauer, Emmett and Teller (BET) specific surface area of HBGN, Msi is the mass of Si film, M_{HBGN} is the mass of HBGN and ρ_{si} is the density of amorphous silicon. The density of amorphous Si and the BET surface area of HBGN in the calculation are 2.26 g/cm^3[106] and 269 m^2/g,[98] respectively. The calculated d values for sample A and B are 101 and 183 nm, respectively. This calculation suggests that there exists minimal void space to accommodate a large volume change of Si without interfering with each other and to avoid high compressive stresses during the Li alloying/de-alloying cycles. This model only takes into account stresses related to the geometrical design of additive-free Si electrodes. If the void space design does not satisfy the relation, the electrochemical performance of the electrode will deteriorate. The stress in the Si thin film originates from the constrained interface between the graphene sheets and the Si film during lithiation/de-lithiation. The stress in the out-of-plane direction can be assumed to be zero, which means that the Si expands freely without constraint.

However, the exposed Si surfaces can be constrained by the adjacent lithiated Si film when they come into contact, which results in a large compressive stress. Furthermore, the Li-ion diffusion path to the Si film will be blocked by the expanded Si, which may lead to limited lithiation and breakdown of the structure. A more systematic investigation on the effect of the void space will be possible with a size-and shape-controlled synthesis of the support structure using a template.

3.4. **Conclusions**

The electrochemical performance of a novel hybrid Si/HBGN was investigated for an anode in LIBs. The Si/HBGN was synthesized through a two-step CVD method: PECVD for HBGN synthesis and LPCVD for Si film synthesis. The hybrid Si/HBGN grown on a stainless steel foil was directly used for an anode without further process. The void space in HBGNs plays a critical role in the electrochemical performance to accommodate the strain relief of the Si film. With proper control of the loading density and the thickness of the Si film, the hybrid Si/HBGN exhibits a reversible specific capacity of 1,740 mAh/g and good cycle performance. Further studies are warranted to better control the growth of HBGNs in an extended area with a larger void space for increased loading density of the Si film.

CHAPTER 4 NOVEL HYBRID SI FILM/CARBON NANOFIBER AS AN ANODE MATERIAL FOR LITHIUM-ION BATTERIES

4.1. Introduction

The performance of lithium-ion batteries (LIBs) greatly depends on the properties of electrodes. Thus, the choice of electrode materials and their structural/morphological characteristics especially in nanometer scale are the critical factors to determine the performance of LIBs.[47, 91, 107] The large stress in the Si materials is generally alleviated by reducing the size of the Si materials. Various types of Si nanostructures such as nanoparticles,[91, 103, 108] nanotubes,[38, 109, 110] nanowires,[47, 111, 112] and nanofilms[113, 114] have been examined as anode electrodes in LIBs to optimize the battery performance toward high energy/power density and long cycle life by controlling the degree of volume change. The nanostructured Si/Si-based electrodes have shown superior performance compared with bulk Si electrodes. However, the challenges of scalability, high cost and a relatively short cycle life remain.

An excellent cycle performance of the Si-based electrode has been achieved when the silicon is used in the form of a few tens of nanometer-thin film since the nano-scale film thickness efficiently mitigates the mechanical stress during the Li alloying/dealloying. The Si film can be synthesized by a low pressure chemical vapor deposition (LPCVD) method,[57, 115] magnetron sputtering,[114, 116] and vacuum evaporation.[41] LPCVD is the most favorable method for conformal deposition of Si on a complex-shaped substrate, which is important for the uniform distribution of the internal stress in Si materials during cycles. The thickness of the Si film is controllable by the SiH_4 flow rate and the growth duration. An excellent cycle performance was demonstrated with 250 nm Si film, while the loading amount of Si thin films on the as-received current collectors was very limited.[117] On the other hand, increasing the loading density by using Si thick film such as 1 µm exhibits poor cycle stability. Several research groups have demonstrated that a chemically or mechanically roughened substrate improves the cycle stability by increasing the adhesion force between the Si film and the substrate.[41, 114] The roughened substrate generates interlocking shapes being filled with Si and holding the Si film more tightly to the substrate.

To increase the loading density of the active materials, a new supporting structure is necessary to provide a large surface area to increase the loading density of Si films, good electrical conductivity to enhance fast electron transfer, and mechanical flexibility to relieve the stress. Wang et al. designed a vertically-aligned carbon nanotube (VACNT) decorated with Si nanoparticles.[94] In a similar fashion, Evanoff et al. synthesized a Si film/VACNT hybrid structure to circumvent the issue and showed excellent loading density and electrochemical performance.[118]

Here, we investigate new hybrid materials based on carbon nanofibers (CNFs) and Si films for stable and high energy-anode materials in LIBs. The novelty of our research is on a facile synthesis process to produce Si- and carbon-based hybrid electrodes by modifying the current collector to favor Si film deposition. The CNFs that serve as a supporting matrix for Si films provide a large surface area, good electrical conductivity, and economical synthesis processes. The electrolyte can easily penetrate a porous CNF network and increase the contact area between the electrolyte and the active materials. Individual CNFs make direct contact with the current collectors, providing a fast and efficient electron transfer pathway.

4.2. Experimental Method

To synthesize CNFs directly on a stainless steel substrate, we modified a CNT growth method described by Baddour et al.[119] High iron and nickel content in type 304 stainless steel (Fe:Cr:Ni=70:19:11 wt.%, Alfa Aesar) facilitates the growth of CNFs.[120, 121] The growth process consists of three steps: acid treatment, heat treatment, and CVD growth. The 25 µm thick stainless steel foil was ultrasonicated in acetone for 30 min. The type 304 stainless steel foil contains a high iron and nickel content (81 % in weight). However, the passive film of chromium (Cr_2O_3) on the surface prevents the carbon precursors in the CVD process from reacting with iron and nickel.[122] To remove the

Cr_2O_3 film, the substrate was etched with 35 wt % hydrochloric acid (HCl) for 10 min. The acid-treated substrate was transferred to the CVD reactor and the thermal annealing was carried out in argon at 850 °C for 30 min. After adjusting the temperature to 700 °C, the CNFs were grown at atmospheric pressure with a gas mixture of acetylene (C_2H_2) containing water vapor and hydrogen (H_2). The gas flow ratio of C_2H_2 and H_2 was fixed at 1:10 during the synthesis. The outlet of the CVD reactor was connected to an oil bubbler to prevent the air from flowing back into the reactor.

Subsequently, Si thin films were deposited on the CNFs using LPCVD. The CVD reactor was sealed and purged with argon three times before increasing the temperature of the reactor. The pressure of the reactor was maintained below 30 Torr for uniform deposition of Si films over the substrate by increasing the mean free path of Si atoms in low pressure. When the temperature of the reactor reached 500 °C, 0.75 % silane (SiH_4, Airgas) in argon (Ar, Airgas) was supplied for a specific time, depending on the desirable thickness of Si films. The weight of the active materials was acquired by measuring the weight change before and after the Si deposition. As-prepared Si/CNF hybrid materials on stainless steel were used for anode electrodes without further treatment. The coin-type half cell (CR2032) was assembled in a glove box under an argon atmosphere with oxygen and moisture levels below 1 ppm. Lithium metal foil was used as the counter and the reference electrodes, and a Celgard 2325 trilayer porous polymer membrane was used as the separator. The electrolyte was composed of a 1 M $LiPF_6$ solution in a carbonate mixture (EC:EMC=40:60 by volume). The electrochemical performance was evaluated at room temperature using a Land Battery Test System in a galvanostatic mode.

4.3. **Results and Discussion**

CNFs were directly grown on type 304 stainless steel foils without applying additional catalysts such as iron deposition onto a substrate. Scanning electron microscopy (SEM) and transmission electron microscopy (TEM) observation were used to investigate the structure of CNFs. Figure 4.1a shows a SEM image of CNFs grown on the stainless steel foil, covering the entire surface of the half-inch substrate in diameter. The CNF network was randomly entangled with diameters in the range from 100 to 400 nm. The diameter of the CNF is directly related to the size of the catalyst particle,[123, 124] indicating a wide range of catalyst size on the stainless steel after the pre-treatment process. The TEM image in Figure 4.1b clearly shows that CNF has the catalyst particle at the tip of the fiber. In Figure 4.1c, the selected area electron diffraction (SAED) pattern on the CNFs shows two concentric diffraction rings that correspond to the (002) and (100) planes of graphite; however, no distinct diffraction spots indicate poor graphitization of CNFs.

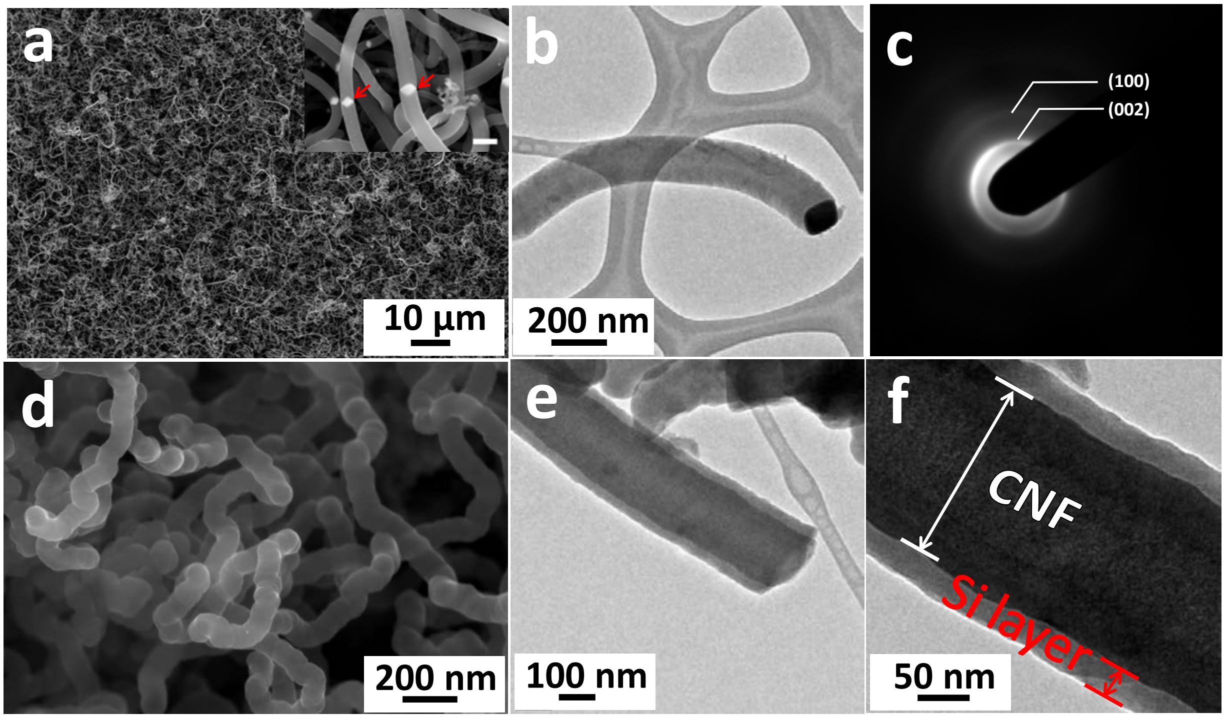

Figure 4.1 (a) SEM image of CNFs grown on type 304 stainless steel foil. Red arrows point at catalyst particles in the inset (scale bar in the inset: 20 nm). (b) TEM images of CNFs. CNFs were synthesized directly on type 304 stainless steel without adding any catalyst. (c) SAED pattern on CNFs. (d) SEM image of Si-deposited CNFs. (e) and (f) TEM images of Si-deposited CNF. TEM images show cylindrical structure with Si coating layer of thickness about 30 nm.

The Si film was deposited on the CNF-grown stainless steel foil via LPCVD, as shown in Figure 4.1d. The hybrid Si/CNF on stainless steel foil was ultrasonicated in ethanol to remove it from the substrate and transferred to the TEM grid. The TEM images of the Si/CNF in Figure 4.1e and f show a distinct layer. The diameter of the CNFs is

~150 nm and increases to ~210 nm after Si film deposition, which indicates the Si film thickness of 30 nm after coating with Si films for 30 min. The presence of amorphous Si film can be observed through XRD and energy dispersive X-ray spectroscopy (EDS) studies.

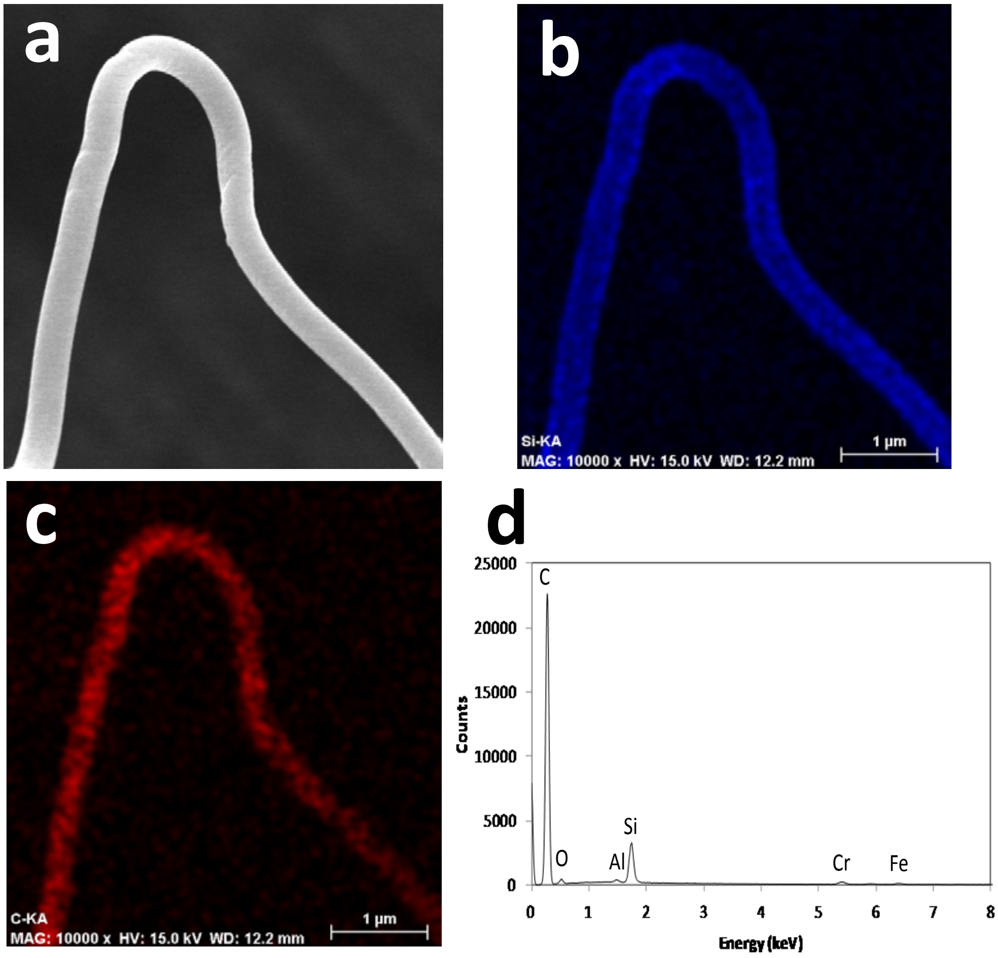

Figure 4.2 (a) SEM secondary electron image, (b) and(c) Elemental maps of Si and C in Si/CNF, respectively, (d) EDS spectra of Si /CNF.

In Figure 4.2a-c, EDS elemental analysis indicates that the Si films were uniformly coated on CNFs. The hybrid materials are composed of Si, C, O and the weak Cr and Fe peaks come from the underlying stainless steel substrate in Figure 4.2d. Si films were also grown on Cu foil for the XRD study.

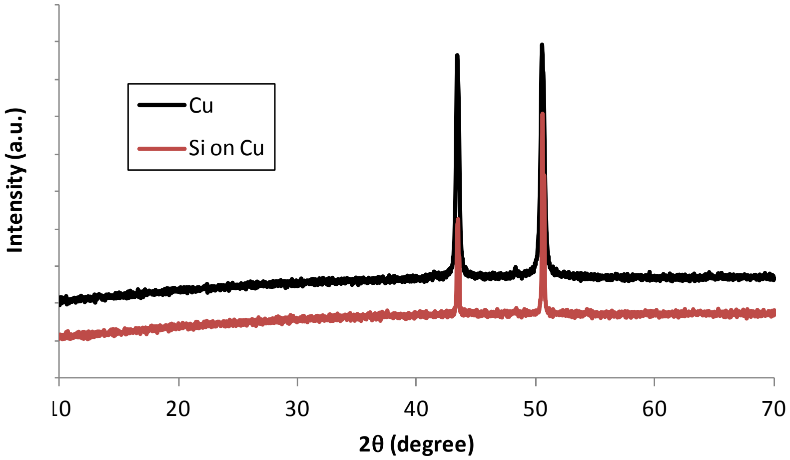

Figure 4.3 X-ray diffraction patterns of Si film on Cu substrate (red line) and Cu substrate alone (black line).

The XRD result shown in Figure 4.3 indicates that Si films were amorphous since there was no obvious difference in the XRD pattern between Cu and Si-coated Cu. The only well-developed peaks were associated with the Cu substrate. Figure 4.4 shows the Raman spectra of the Si/CNFs hybrid and CNFs. The Raman spectrum of the Si/CNF displays three well-defined peaks, a main peak at around 510 cm^{-1} responsible for Si film (not shown in the CNF sample), and two more peaks at 1360 cm^{-1} (defect-induced D band) and 1590 cm^{-1} (in-plane vibrational G band), typical for graphitic carbon. Carbon coating on the as-produced Si/CNF composites was used to achieve for stable electrochemical performance.

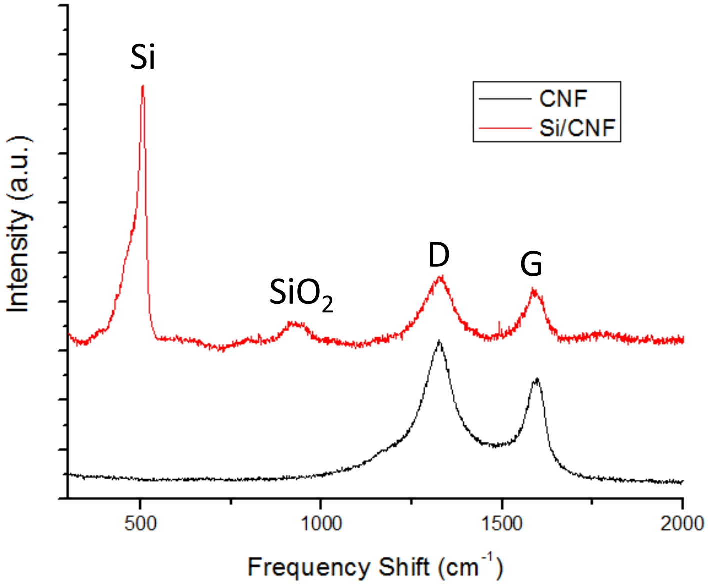

Figure 4.4 Raman spectra of CNFs before and after Si film deposition (red line: Si/CNF, black line: CNF).

The electrochemical test was performed using the hybrid Si/CNF as a working electrode and lithium metal as a counter electrode. The specific capacity and Coulombic efficiency (CE) of the Si/CNF electrode vs. the cycle number are shown in Figure 4.5a. In this study we defined the charging and discharge processes as de-lithiation and lithiation of Si, respectively. The Si/CNF exhibited high capacities with excellent cycle stability, which was possibly due to the stress-resistant nature of the Si thin film, the robust mechanical support, and the good electrical properties of CNFs. The nanometer-thin layer of the Si films allows fast diffusion of the Li-ions to the core of the active materials. The weight ratio of Si film to CNF was about 1:1. The contribution of the Li intercalation to the CNFs is less than 10 % of total capacity in the hybrid materials according to the theoretical capacity of Si and C, even when C is fully intercalated; thus, the specific capacity was calculated using the mass of Si. The cells were galvanostatically cycled at a low current rate of 0.05 C (1C=2,000 mA/g) between 0.01-2 V (vs. Li/Li^+) for the first three cycles to ensure a stable SEI film formation and a rearranged electrode structure due to the large volume changes during initial Li alloying/de-alloying. The current rate was increased to 1 C for the remaining cycles over the voltage window 0.05-1.5 V to limit the state of discharge.

The reversible charge (de-lithiation) capacity of the Si /CNF was about 1,000 mAh/g over 200 cycles. There was a slight increase in the specific capacity from 10 to 80 cycles that resulted from increasing the Si atoms in activation.

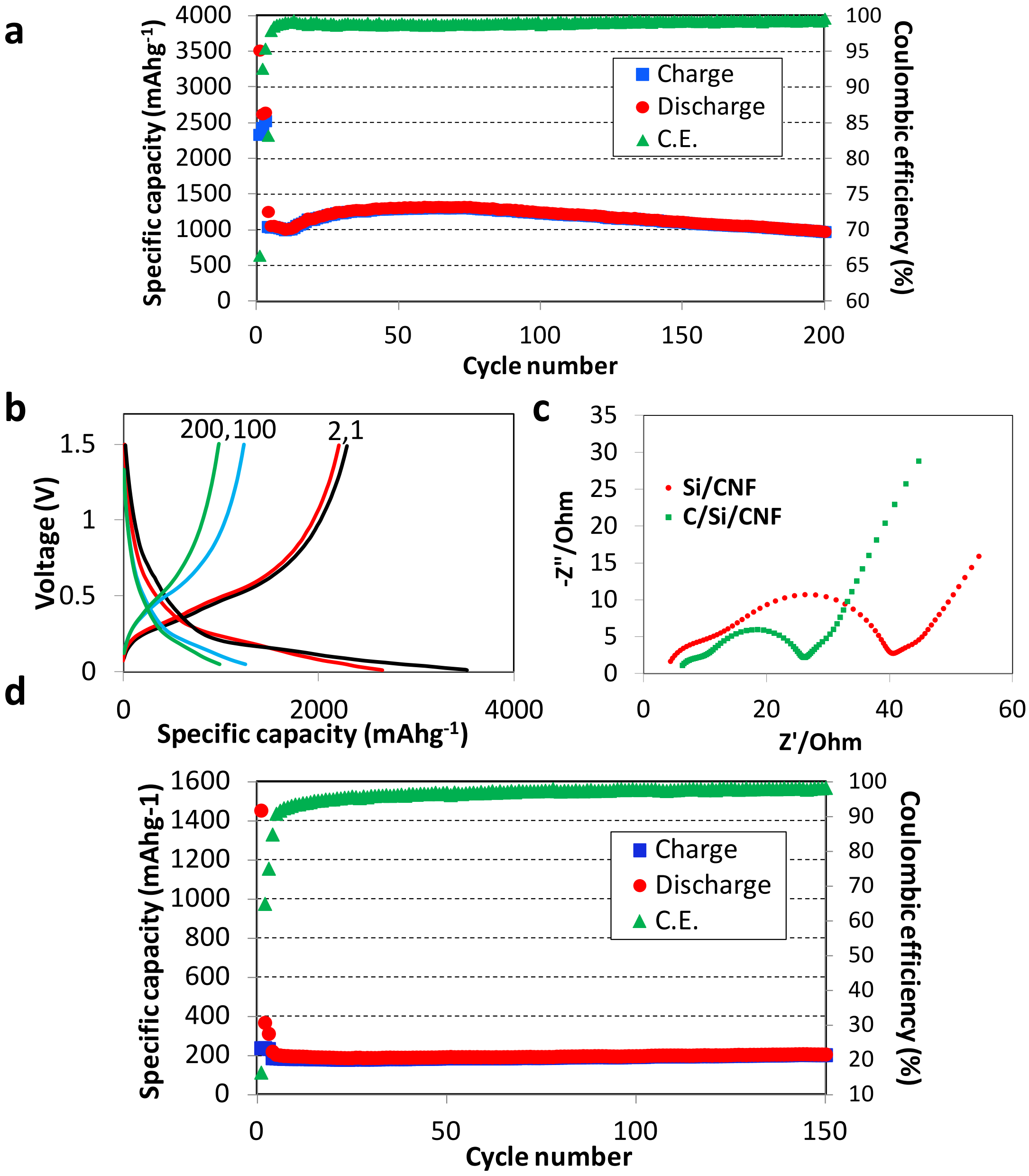

Figure 4.5 (a) Cycle performance (charge, discharge, and Coulombic efficiency or CE) of Si/CNF electrode between 0.01 and 2.0 V at a current rate of 0.05 C (or 100 mA/g) in the first 3 cycles, and between 0.05 V and 1.5 V at a current rate of 1 C (or 2,000 mA/g) for the rest of the cycles. (b) Galvanostatic charge/discharge profiles of Si/CNF electrode at a current rate of 0.05 C in the first 3 cycles, and 1 C for the rest of the cycles for Si/CNF

electrodes. (c) Nyquist plot of Si/CNF electrode before (blue circle) and after carbon deposition (red square). (d) Cycle performance of CNF alone electrode between 0.01 and 2.0 V at a current rate of 0.5 C (or 150 mA/g) in the first 3 cycles, and 1 C (or 300 mA/g) for the rest of the cycles.

The major reason for the excellent cycle performance is ascribed to the structural integrity of the Si thin film without much degradation. On the other hand, the capacity fade started slowly around 80 cycles, which may be attributed to the delamination of the Si thin film from the CNF surface and the disintegrated SEI film after the repeated volume change of the Si film. Figure 4.5b shows typical galvanostatic charge/discharge profiles of the Si/CNF electrode at the current rate of 0.05 C in the first 3 cycles, and 1 C for the rest of the cycles. The specific charge/discharge capacities of the hybrid electrodes are 3,522 mAh/g and 2,341 mAh/g, respectively, which indicates that the initial CE of the hybrid electrodes was ~66 %. There is an obvious difference between the first discharge curve and the second one. The irreversible capacity in the first cycle is caused by the reductive decomposition of the electrolyte solution and the subsequent SEI film formation. After a few cycles, a high CE of >99 % was achieved in the remaining cycles. In the first discharge (Li alloying with Si) voltage profile, the voltage drops quickly to 0.3 V and gradually decreases to 0.01 V. The long plateau near 0 V is attributed to the lithium alloying with silicon and to form Li_xSi. The 100th and 200th charge/discharge profiles are very similar except for a slight capacity loss, suggesting that the hybrid materials retain their structure without distinctive degradation.

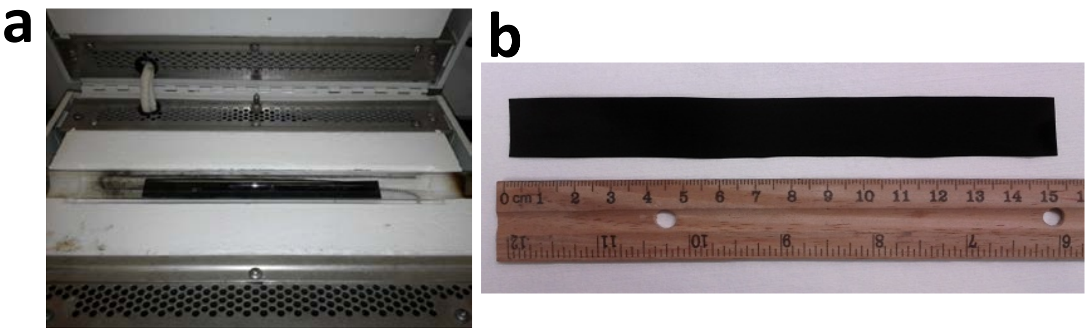

Figure 4.6 CNFs grown on stainless steel foil. (a) CNF-grown stainless steel foil in CVD reactor. (b) CNFs are totally covered on both sides of stainless steel foil with a size of 15 ×150 mm.

Several studies reported that carbon coating on Si-based electrodes is an effective way to improve their electrochemical properties by suppressing the large consumption of electrolytes to form SEI film and providing more conductive networks in the active materials while Li ion is permeable.[103, 104, 125, 126] The Nyquist plot was used to verify the improved electrical conductivity of the Si/CNF hybrid electrode by applying carbon coating on the surface of the Si film. In Figure 4.5c, the electrochemical impedance spectroscopy (EIS) tests were conducted on both electrodes in fully delithiated state after completing two charge/discharge cycles. The Si/CNF electrode with carbon coating exhibits a smaller semicircle at the medium-frequency zone, suggesting a smaller charge transfer resistance on the electrode/electrolyte compared with that of the Si/CNF electrode.

As a comparison, the control electrodes were assembled and tested with CNFs alone. It was found that the specific capacity of CNFs only was approximately 200 mAh/g at the current rate of 300 mA/g, much smaller than that of the hybrid electrodes as shown in Figure 4.5d; however, the CNF electrodes showed extremely stable cycle performance without distinctive degradation of capacity over 150 cycles. Considering the simple fabrication methods of CNFs, it is very promising to use a CNF electrode directly as an anode electrode without adding any conductive agents and polymeric binders.

In Figure 4.6, uniform CNFs were grown on both sides of 15 mm by 150 mm stainless steel foil whose size is only limited by the dimension of the tube furnace. Large-scale production of CNF electrodes is readily possible with an increased reactor size. However, the as-produced CNFs exhibit high irreversible capacity loss in the first cycle, which may be attributed to irreversible Li-ion reaction with the oxygen-containing function group. Further research on reduction/electrochemical characteristics of CNF electrode is needed. The rate performance of the hybrid Si/CNF was tested at various current rates as shown in Figure 4.7. The reversible discharge capacity reached 2,815 mAh/g, 2,149 mAh/g, 1,487 mAh/g, and 767 mAh/g at the current rate of 0.5 C, 1 C, 2 C, and 5 C, respectively. The excellent rate capability is attributed to the short distance for Li-diffusion and electron transfer in the Si thin films.

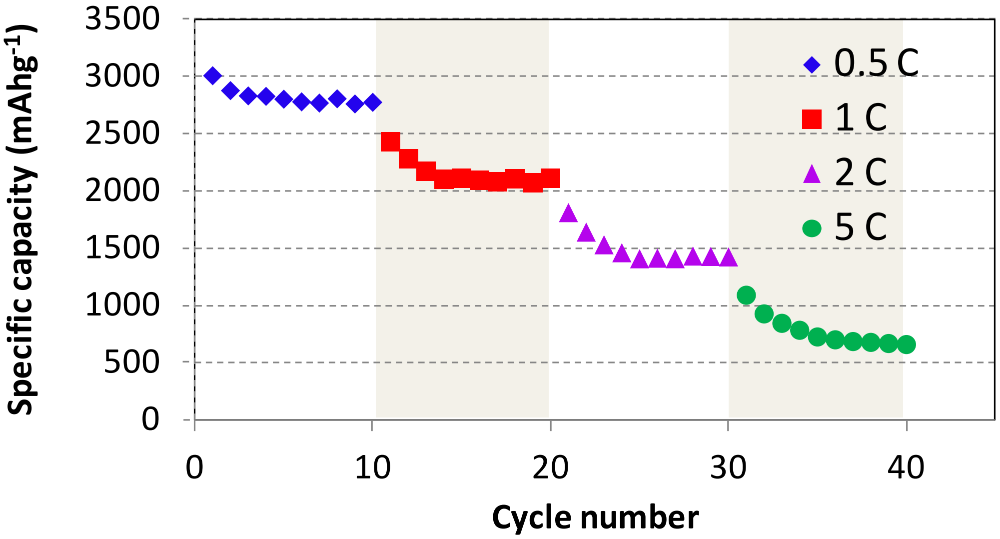

Figure 4.7 Rate capability of the hybrid Si/CNF at various current densities between 0.5 and 5 C. The coin cell was cycled at 0.05 C in the first 3 cycles before the rate performance test.

The electrode materials in LIBs undergo repeated volume changes during charge/discharge cycles leading to pulverization of the materials. To better optimize the design of the Si film anodes for a long cycle life, a fundamental understanding on the structural change of the Si electrode is required. Here we investigate the critical thickness of the Si film on CNFs by using fracture mechanics. The mathematical analysis focuses on the mechanical failure due to the lithiation-induced stress in Si materials, but excludes any other battery degradation factors such as chemical degradation caused by SEI layer formation.

Table 4.1 Parameters for the calculation of a critical crack size in a thin film.

Parameter	Symbol	Value	Ref
Young's modulus	E	80 Gpa	[127]
Fracture energy	Γ	5.4 J/m	[128]
Yield stress	σ_Y	1.75 GPa	[129]
Dimensionless coefficient	Z	2	[130]
Radius of CNF	A	100 nm	
Radius of fully-lithiated Si	b	370 nm	

In this calculation, the radii of the CNF (A) and fully-lithiated Si (b) are 100 and 370 nm (Figure 4.8), respectively. The fracture energy is a material property, a resistance to the further development of the crack. The lithiated Si film may increase the thickness of the film up to 3.7 times due to the constrained bottom surface. The critical size of crack, also known as Griffith flaw is calculated. With the assumption that the Si film has initial crack that is much smaller than the thickness of the film, the energy release rate (G) can be expressed as follows [130, 131]:

$$G = Z\frac{\sigma^2 a}{E} \qquad \text{Eq. (4.1)}$$

where Z is a dimensionless coefficient that is a function of Young's modulus ratio of the film and the substrate, a is the characteristic length and E is Young's modulus. The critical thickness of the film (t) is determined by taking a/t ≈ 1. The energy release rate is related to the applied force that may trigger the further development of the crack. The crack size will grow further when the energy release rate is equal to or higher than the fracture energy *Γ*. That is when the structure is fractured. The fracture will break the atomic bonding and leave a plastic deformation in the materials.

$$G \geqq \Gamma \qquad \text{Eq. (4.2)}$$

The lithiation-induced stress field of Si films on the cylindrical shell was derived by Wang et al.[132] using the continuum theory of finite deformation.

$$\sigma_r = \frac{\sqrt{3}}{3}\sigma_Y\left(2\log\frac{b}{r} + \log\frac{\sqrt{r^4+3A^4}-\sqrt{3}A^2}{\sqrt{b^4+3A^4}-\sqrt{3}A^2}\right) \qquad \text{Eq. (4.3)}$$

$$\sigma_\theta = \frac{\sqrt{3}}{3}\sigma_Y\left(2\log\frac{b}{r} + \log\frac{\sqrt{r^4+3A^4}-\sqrt{3}A^2}{\sqrt{b^4+3A^4}-\sqrt{3}A^2}\right) + \frac{2\sigma_Y}{\sqrt{\frac{r^4}{A^4}+3}} \qquad \text{Eq. (4.4)}$$

$$\sigma_z = \frac{\sqrt{3}}{3}\sigma_Y\left(2\log\frac{b}{r} + \log\frac{\sqrt{r^4+3A^4}-\sqrt{3}A^2}{\sqrt{b^4+3A^4}-\sqrt{3}A^2}\right) + \sigma_Y\left(\frac{1}{\sqrt{r^4/A^4+3}} + \frac{1}{\sqrt{1+3A^4/r^4}}\right) \qquad \text{Eq. (4.5)}$$

The stress distributions are plotted in Figure 4.9, suggesting that the axial stress is the dominant stress component. We also learn that the radial stress (σ_r) is relatively smaller than the hoop stress (σ_θ) and the axial stress (σ_z). The radial stress becomes largest at the interface due to the constrained bottom surface and becomes zero at the free surface.

Using the Eq. (4.1), Eq. (4.2) and Eq. (4.5), the critical thickness can be rewritten as

$$a = \frac{\Gamma E/Z}{\left(\frac{\sqrt{3}}{3}\sigma_Y\left(2\log\frac{b}{r} + \log\frac{\sqrt{r^4+3A^4}-\sqrt{3}A^2}{\sqrt{b^4+3A^4}-\sqrt{3}A^2}\right) + \sigma_Y\left(\frac{1}{\sqrt{r^4/A^4+3}} + \frac{1}{\sqrt{1+3A^4/r^4}}\right)\right)}$$

Eq. (4.6)

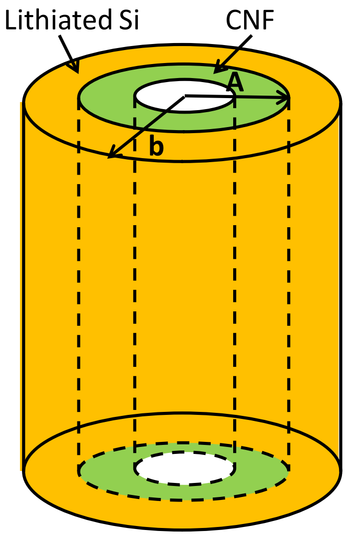

Figure 4.8 Diagram of CNF/lithiated Si film. A and b are radius of CNF and lithiated Si, respectively.

The axial stress will generate a circumferential crack. The critical thickness of the film will be acquired when the axial stress attains its maximum value. By substituting the maximum value of σ_z, dimensionless coefficient, and fracture energy from Table 4.1 into Eq. (4.1), we can obtain the critical thickness of the Si film as 52.0 nm. The fracture in the Si film will occur in the circumferential direction if the film thickness is larger than 52.0 nm.

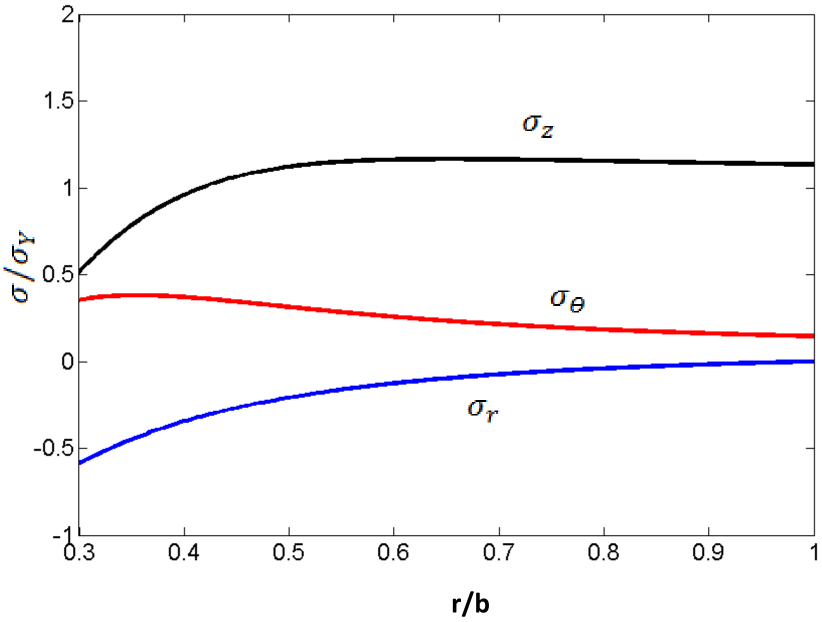

Figure 4.9. Stress distribution of radial, hoop, and axial direction in the Si film.

4.4. **Conclusions**

In summary, the novel Si/CNF hybrid materials were obtained by a two-step CVD method. The hybrid materials incorporating CNFs with a large surface area and Si films with a high lithium storage capacity showed a highly reversible capacity of about 1,000 mAh/g over 200 cycles. The electrochemical results are very promising and provide a possible approach for practical LIB anode. The poor capacity retention of Si electrodes was effectively addressed by combining the advantageous features of CNFs and Si film: (1) a strong mechanical structure for extended cycle performance, (2) efficient pathways for Li-ion diffusion and electron transfer, (3) stress-resistant Si thin film with excellent cycle stability. To better optimize the cycle performance of the Si/CNF electrodes, further characterizing the hybrid nanostructures, understanding the interface between Si thin films and substrates, and illuminating the aging mechanism of Si thin films would be necessary.

CHAPTER 5 NOVEL HYBRID CARBON NANOFIBER/HIGHLY BRANCHED GRAPHENE NANOSHEET AS AN ANODE MATERIAL FOR LITHIUM-ION BATTERIES

5.1. Introduction

Nanostructured carbon exists in various types of allotropes: 0-dimensional fullerenes (C60), 1-dimensional carbon nanotubes (CNTs) and carbon nanofibers (CNFs), and 2-dimensional graphenes (or GNS: graphene nanosheet). Each carbon allotrope that is characterized by its unique shape, dimensionality, and properties can be used as a building block to synthesize new hybrid materials by combining two or more allotropes.[133] Novel hybrids with a new structure and new morphology can be realized by two representative methods: (1) mixing surface-treated carbon materials[134-136] and (2) employing catalytic seeds for 1D carbon growth on 2D graphene.[137, 138]

Among these carbon allotropes, the recent discovery of the wonder material graphene has totally changed our view of the nanoscopic world, owing to its special structure and properties.[23, 139] Graphene is a one-atom-thick 2D sheet of sp^2-bonded carbon atoms having exceptional mechanical, electrical, and thermal transport properties.[140-142] In particular, graphene exhibits remarkably high electron mobility even at ambient temperatures.[143, 144] Graphene can be produced by exfoliating graphite,[145, 146] epitaxial growth from a SiC single crystal surface,[147, 148] solvothermal reaction,[149] and chemical vapor deposition (CVD).[141, 150, 151] There have been various approaches to take advantage of the unique properties of graphene in opto-electronics,[152, 153] sensing[154, 155] and energy storage.[28, 156-158] Recently, Chae et al. designed a new hybrid of CNT/graphene integrated with a winkled Al_2O_3 layer, demonstrating great potential for stretchable and transparent electronics.[159] Kim et al. developed a superelastic and fatigue-resistant 3D-CNT network by coating it with a few layers of graphene, which improves the Young’s modulus by a factor of 6.[160] Previously, our group reported a CNT hybrid material covalently bonded with graphene leaves[161] and highly branched graphene nanosheets (HBGNs) directly grown on a planar graphene sheet.[98] HBGNs are a few layered graphene nanosheets with open boundaries, which have similar structural characteristics to carbon nanowalls (CNWs). However, different from CNWs, HBGNs are composed of a highly dense, small graphene domain with less than 5 nm in lateral dimension, and the “standing” graphene sheets are randomly oriented.

In this study, we investigate novel hybrid CNF/HBGN for anode materials for LIB application. HBGNs can be grown on any electrically conductive substrate without adding any catalyst. We used direct growth of CNFs on type 304 stainless steel for hybridizing with HBGNs. In contrast to the loosely bound hybrids prepared by simply mixing two materials or catalytic growth on a graphene surface, the hybrid CNF/HBGN will provide a continuous conduction pathway, which is expected to lead to a high charge carrier mobility. CNFs will offer good electrical conductivity and a robust support structure, while HBGNs offer increased Li storage sites. The controlled synthesis method for hybrid CNF/HBGN will offer insights into the bottom-up design of carbon-carbon bond formation.

5.2. Experimental Method

The CNF/HBGN synthesis is accomplished through a two-step CVD process. The experimental details can be found in Chapter 2-4. In brief, the two-step CVD process consists of a CVD method for CNF growth and a plasma-enhanced CVD (PECVD) method for HBGN growth, both of which were catalyst-free atmospheric pressure growth. We modified a CNT growth method described by Baddour et al.[119] to synthesize CNFs. The CNF growth was conducted without applying additional catalysts that are generally required to nucleate CNFs through C atom diffusion over the catalyst. CNFs were directly grown on type 304 stainless steel (Fe:Cr:Ni=70:19:11 wt.%, Alfa Aesar) that contains a large fraction of iron and nickel. To facilitate the growth of CNFs, the surface condition of stainless steel needs to be modified to create particle-like active catalytic sites. In this pretreatment step, the native passive oxide film (Cr_2O_3) was etched away with 35 wt.% hydrochloric acid (HCl) for 10 min. This etching process can be replaced by mechanically polishing the surface of stainless steel without difficulty since the passive oxide layer is only a few nanometers thick.

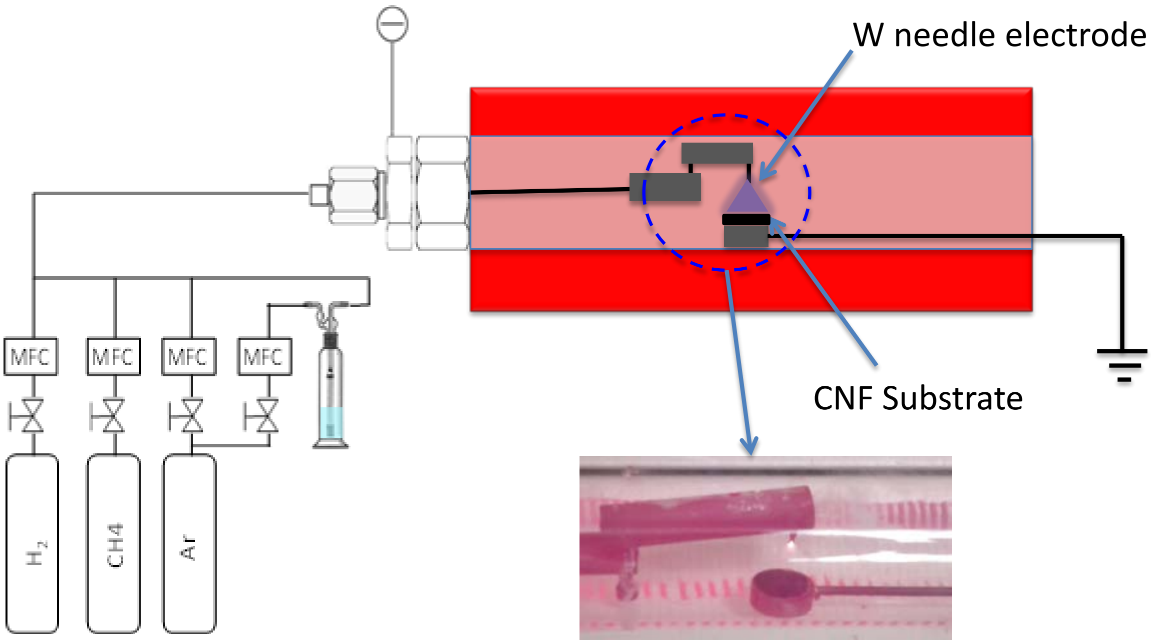

Figure 5.1 Experimental setup for CNF/HBGN growth using PECVD at atmospheric pressure. The bottom photo in the figure shows a tungsten needle electrode pointing in the direction of the CNF substrate sitting on a disc electrode, generating a glow discharge between the electrodes.

Next, the acid-treated stainless steel was thermally annealed for 30 min at 850 °C in a tube furnace under hydrogen environment. The temperature of the reactor was decreased to 700 °C, and the CNF started to grow under the acetylene, hydrogen and water-containing argon flow. Subsequently, HBGNs were synthesized on the CNF substrate using an atmospheric-pressure direct current (dc) PECVD method as shown in Figure 5.1. A pin-plate electrode in a quartz tube reactor was equipped with high voltage supply. The two electrodes, separated by about 10 mm, were installed perpendicular to the flow direction, which did not require any conductive paste or fixture to hold the sample. A mixture of acetylene (C_2H_2) and argon (Ar) with water vapor was introduced into the quartz tube in the reactor. The typical flow ratio of C_2H_2 to Ar was 10 and the temperature of the reactor was 700 °C. When a dc voltage of about 3 kV was applied, the dc glow discharge was formed between the electrodes and HBGNs started to grow on the surface of CNFs.

The CNF/HBGN on stainless steel was transferred to the glove box (H_2O and O_2 level below 1 ppm) for coin cell assembly. The as-produced CNF/HBGN on stainless steel was used as an electrode without binder or conductive additives. The total weight change of CNF/HBGN (loading density: ~0.3 mg/cm^2) on stainless steel was measured for capacity calculation before and after the two-step CVD process. A 2032 coin type half-cell was assembled for electrochemical tests with a working electrode, a Celgard 2322 membrane separator, and Li foil as a reference and counter electrode. The electrolyte consisted of 1 M $LiPF_6$ in a nonaqueous solution of ethylene carbonate (EC) and ethyl methyl carbonate (EMC) of 40:60 volume ratio.

The electrochemical charge-discharge cycles were tested at a LAND CT2001A workstation. Scanning electron microscopy (SEM) analysis was performed on a Hitachi S-4800 SEM with a stated resolution of 1.4 nm operated at 1 kV acceleration voltage. Transmission electron microscopy (TEM) analysis was conducted on a Hitachi H 9000 NAR TEM, which has a stated point resolution of 0.18 nm operated at 300 kV in the phase contrast, high-resolution TEM (HRTEM) imaging mode. Brunauer-Emmet-Teller (BET) specific surface area was measured with a Micromeritics ASAP 2020 using the N_2 adsorption at the temperature of liquid nitrogen. Raman measurements were taken using a Reinshaw 100B with a spot diameter of 4 μm and an excitation wavelength of 633 nm.

5.3. **Results and Discussion**

Type 304 stainless steel contains a high content of iron and nickel, which were used as catalysts to grow CNFs without an additional process to deposit catalysts. In Figure 5.2a, the SEM image shows the clean surface of as-received stainless steel foil. The stainless steel foil was chemically/thermally treated to facilitate the catalyst island formation on the surface.

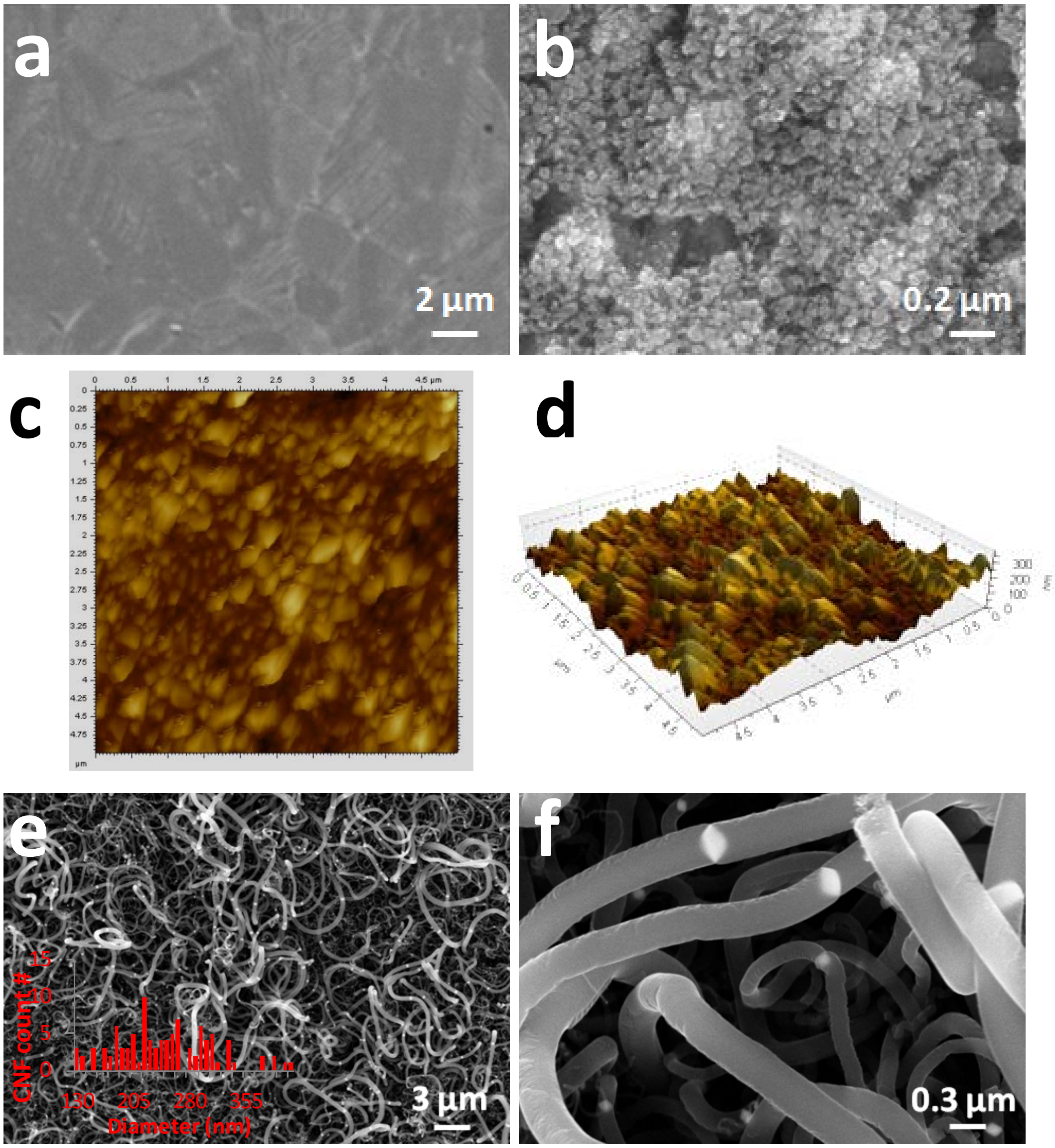

Figure 5.2 (a) SEM image of as-received stainless steel. (b) SEM image of stainless steel after chemical/thermal treatment. (c) and (d) AFM topography images of stainless steel after chemical/thermal treatment. (e) SEM images of CNFs grown on stainless steel. Inset shows the histogram of the CNF diameter. (f) SEM images of CNFs grown on stainless steel at a higher magnification.

After chemical/thermal treatment, particle-like catalysts were precipitated on the stainless steel as shown in Figure 5.2b. The diameter of CNFs is closely associated with the size of the catalyst. The wide diameter distribution of CNFs is attributed to the wide size distribution of precipitated catalyst particles (Figure 5.2c and d). In Figure 5.2e, highly dense CNFs grew intertwined with diameters in the range of 100 – 400 nm (see inset histogram of CNF diameter). Figure 5.2f shows diamond-shaped catalyst particles located in the middle of the CNF. The CNF continues to grow in two opposite directions on the catalyst face. CNF is an ideal platform for bridging the current collector and active materials, since all CNFs are directly connected to the stainless steel and provide robust mechanical support for the HBGNs.

The morphology of HBGNs is very different from solution-grown graphene, which usually forms a wrinkled paper-like structure. After synthesizing HBGNs on the surface of the CNFs, the diameter of the hybrid was increased. The BET surface area for the CNFs and HBGNs was found to be 65 and 269 m^2/g,[98] respectively. The surface area of CNFs was increased by the fusion with HBGNs. Figure 5.3, a high resolution TEM image reveals no long range order in the CNFs suggesting incomplete graphitization, while the HBGNs shows ordered graphite lattices, indicating the HBGNs are composed of a few layers of graphene.

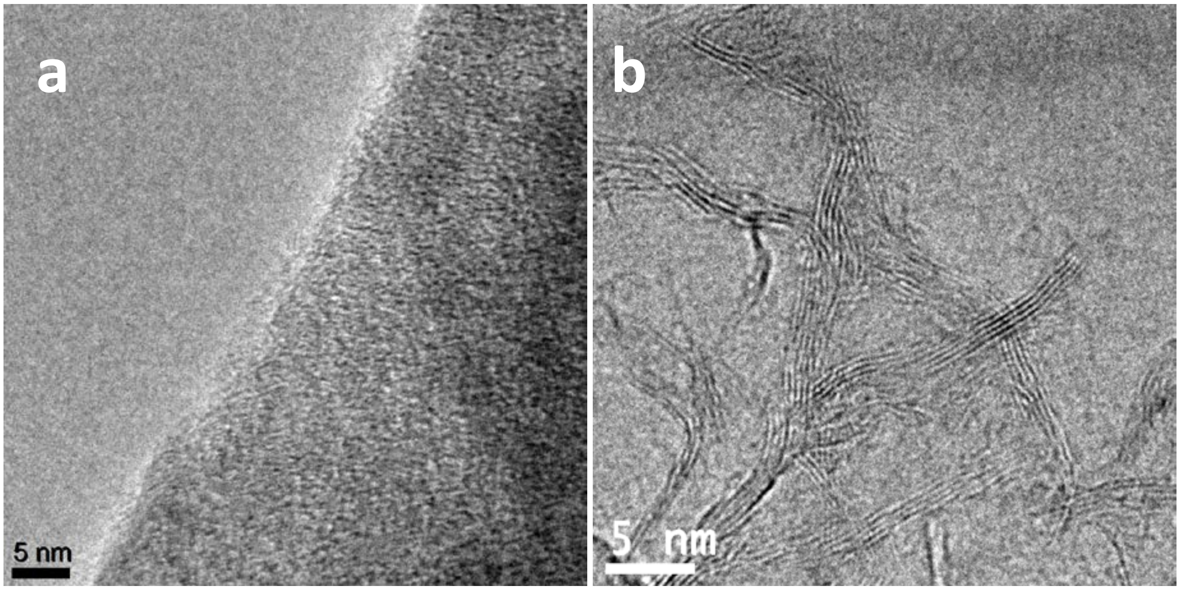

Figure 5.3 High-resolution TEM images of (a) CNFs and (b) HBGNs.

The SEM image in Figure 5.4a-d clearly shows that the HBGNs totally cover the entire external surface of the CNFs, exposing the edge of the graphene platelet. The diameter of the CNF/HBGN gets thicker at the tip of the CNFs because of the enhanced electric field at the tip. Likewise, denser CNF/HBGNs were observed on the top surface of the electrodes as shown in Figure 5.4c.

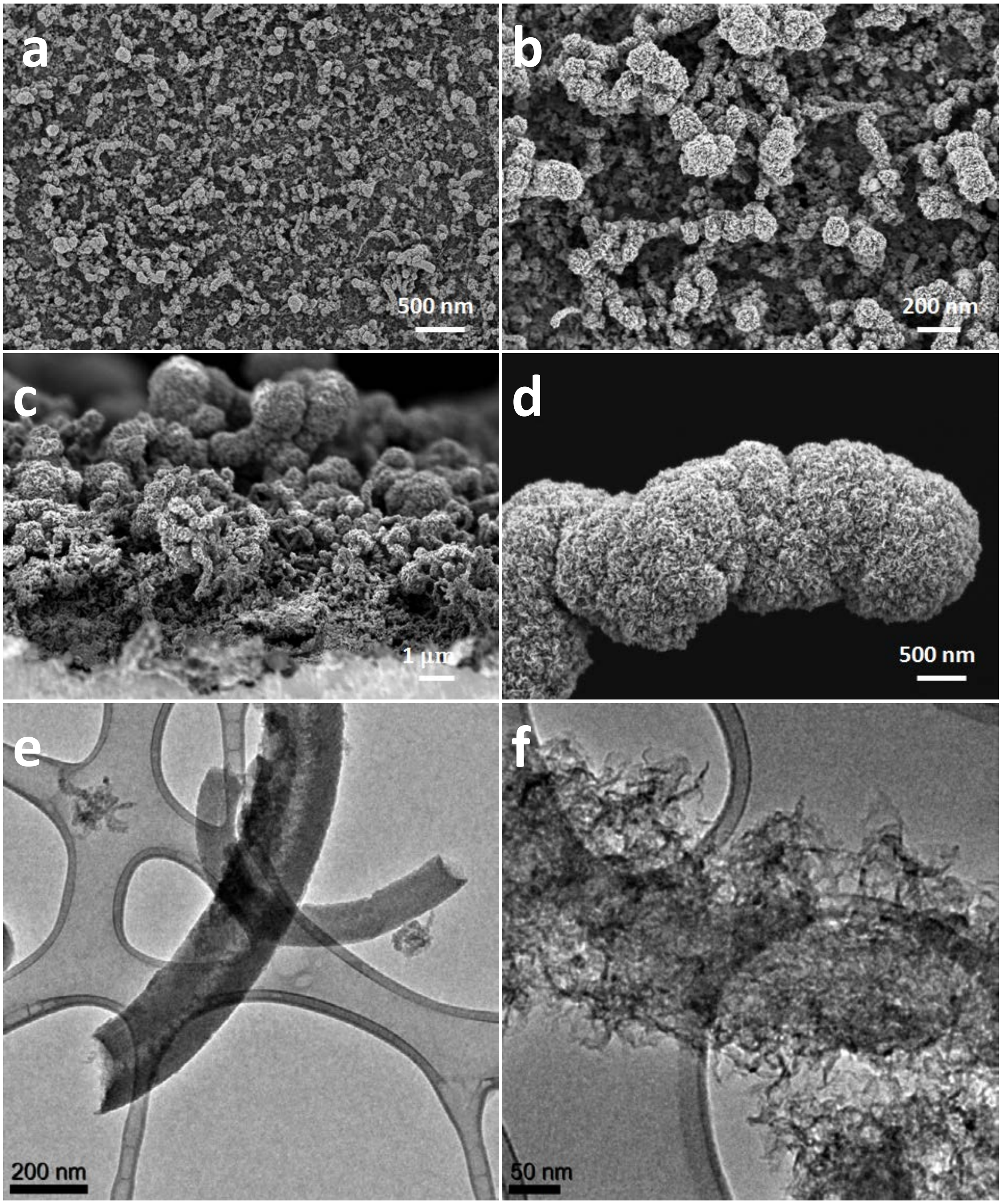

Figure 5.4 (a) and (b) SEM images of CNF/HBGN on stainless steel (top view). (c) and (d) SEM images of CNF/HBGN on stainless steel (side view). (e) TEM image of a bare CNF. (f) TEM image of a CNF/HBGN hybrid.

Figure 5.4e shows a TEM image of the smooth surface of bare CNFs. After ultra-sonication of the CNF/HBGNs for 1 hr, the hybrid was transferred onto the TEM grid. The surface of the CNF was still covered by graphene sheets, proving that there is strong adhesion between CNF and HBGN as shown in Figure 5.4f. The strong adhesion may be attributed to the chemical bonding between a CNF and a HBGN.

Raman spectroscopy was used to investigate the structural properties of the CNF/HBGN hybrid. Figure 5.5 shows the representative Raman spectra of CNF, HBGN and CNF/HBGN having characteristic D band and G bandThe D band is related to the structural disorder of graphite, and the G band is ascribed to in-plane sp^2 carbon atom vibration, indicating the formation of graphitized structure. The Raman spectrum of the CNFs displays two prominent peaks at 1,327 and 1,598 cm^{-1}. After the deposition of HBGNs on CNFs, those peaks shifted to 1,325 and 1,603 cm^{-1}, similar to those seen for HBGNs. Furthermore, the 2D peak at 2,659 cm^{-1} and S3 peak at 2,905 cm^{-1} appeared, indicating the presence of graphitized structure. However, the intensity ratio of D and G bands (I_D/I_G) for HBGN and CNF/HBGN increased to about 2.2, whereas the I_D/I_G for CNFs is about 1.4. The increase in I_D/I_G suggests that the degree of disorder in the hybrid increased by combining the CNFs with the HBGNs. On the other hand, owing to the unique structure of the HBGNs, the presence of graphene edges that are perpendicular to the substrate can be seen as defects, which may contribute to the increased intensity of the D peak to some degree.[162] When the laser beam is on the graphene edge or when the incident light polarization and the edge are parallel, the D peak intensity becomes strong.

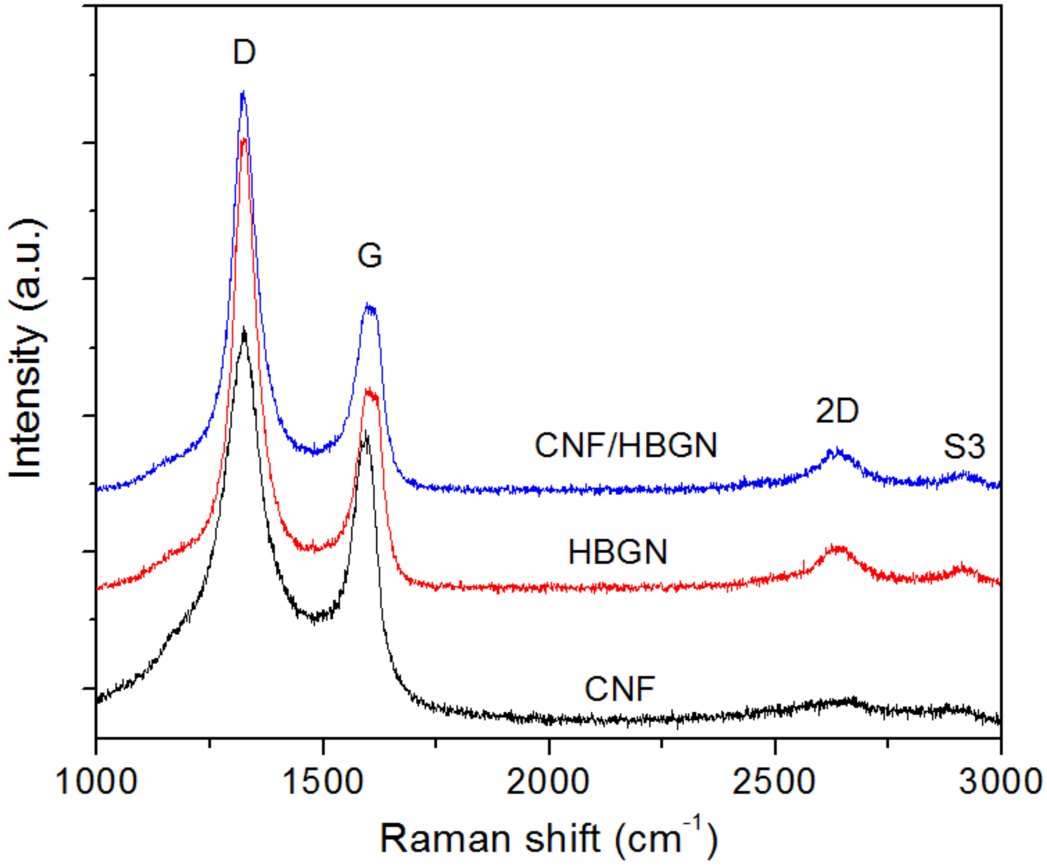

Figure 5.5 Raman spectra of CNF, HBGN and CNF/HBGN.

XPS analysis was conducted in order to investigate the surface condition of the acid treated stainless steel. The passive film of chromium oxide on the surface of stainless steel was removed after etching in 35 wt.% HCl as shown in Figure 5.6. XPS results also indicate the iron oxide (Fe $2p_{3/2}$ peak at 711 eV for Fe^{3+}) decreased significantly after acid etching due to the removal of the iron oxide passive film, which was dominant on the top surface of the stainless steel.[163]

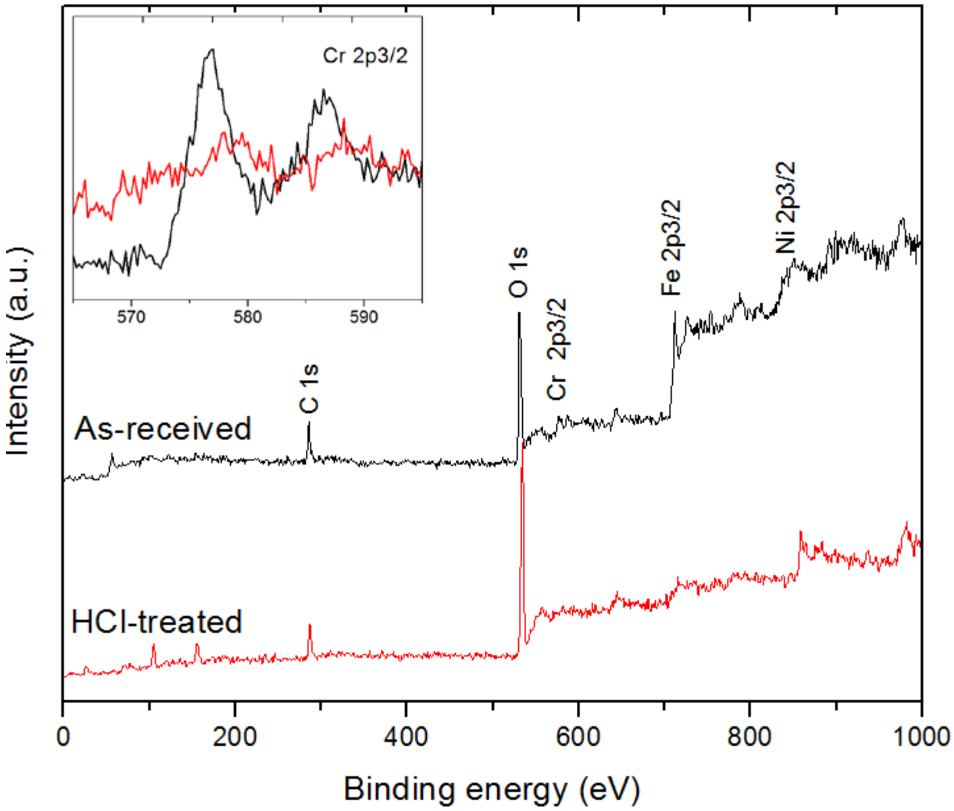

Figure 5.6 XPS analysis of stainless steel before and after HCl treatment for 10 min.

We also confirm that there was no CNF growth on non-treated stainless steel as opposed to the very dense black CNF growth on the acid treated surface in Figure 5.7. The patterned growth of CNF/HBGNs is possible by selectively treating the stainless steel substrate in an acid solution. The CNF/HBGN hybrid was investigated as an anode material for use in LIBs. The electrochemical performance of the CNF/HBGN electrode was tested through a galvanostatic charge (de-lithiation)/discharge (lithiation) cycle.

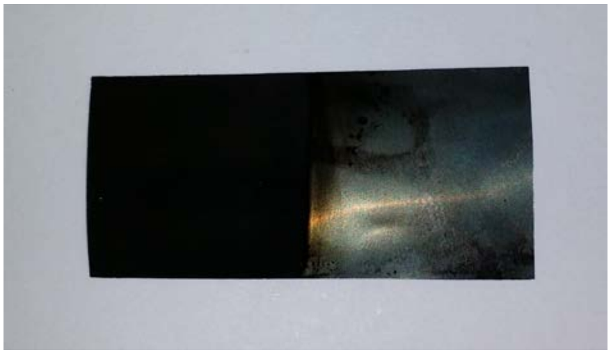

Figure 5.7 CNF covered on the acid treated (left half) and no CNF observed on the untreated (right half) stainless steel foil.

In Figure 5.8a, the cycling performance results showed slight improvement in energy density on the CNF/HBGN electrode compared to CNF alone. The increase in energy density may be attributed to the increased surface area of the hybrid materials. The reversible capacity of the CNF/HBGNs after 200 cycles stayed at about 300 mAh/g, while the reversible capacity of CNF alone after 150 cycles was about 200 mAh/g.

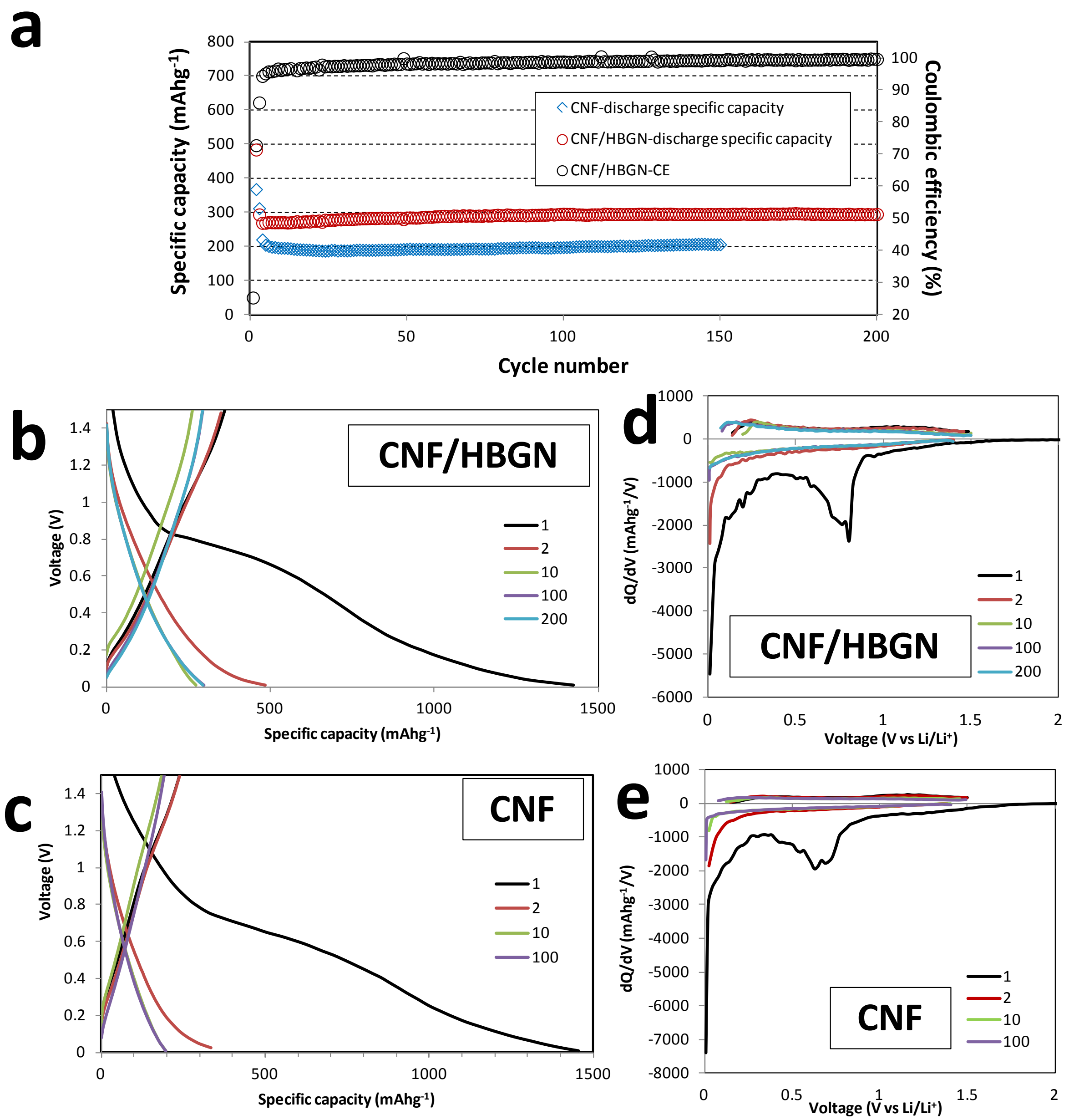

Figure 5.8 (a) Cycle performance (charge, discharge, and Coulombic efficiency or CE) of CNF/HBGN and CNF electrodes between 0.01 and 1.5 V at a current rate of 0.5 C (or 150 mA/g) in the first 3 cycles, and 1 C (or 300 mA/g) for the rest of the cycles. (b) Charge/discharge profiles of CNF/HBGN. (c) Charge/discharge profiles of CNF. (d) Differential capacity (dQ/dV) profiles of CNF/HBGN. (e) Differential capacity (dQ/dV)

profiles of CNF.

Figure 5.8b and c show the charge/discharge profiles of the CNF/HBGN and the CNF electrode, respectively. The Li intercalation behavior of these electrodes was very similar to each other, but different from that of a conventional graphite electrode. The capacity above 0.5 V is attributed to the faradic capacitance on the surface and edges of the graphene, and the capacity below 0.5 V is due to the Li intercalation into the graphene layers.[89] The discharge voltage profiles did not show a distinct plateau below 0.5 V, which is different from the Li-intercalation into graphite, which exhibits a plateau at about 0.1 V.[9] These results indicate that the electrodes may be composed of disorderly stacked graphene sheets.[28] The electrodes exhibited very low Coulombic efficiency (CE), about 25 % in the first cycle due to the SEI layer formation on a large surface area, and an irreversible reaction with amorphous carbon impurities and the oxygen-containing functional groups. The electrochemical reactivity was examined by the dQ/dV profiles, which were acquired by numerical differentiation of the galvanostatic cycling data. The SEI formation is clearly evidenced by large peaks at around 0.8 V in Figure 5.8d and e, which disappeared in the subsequent cycles. It should be noted that there was no measurable weight change on the CNF substrate after ½ hr of HBGN growth, indicating that the amount of HBGNs was less than 0.005 mg. Uncertainty in the specific capacity calculation according to the precision of the balance (Sartorius CPA225D with a precision of 0.01 mg) was estimated to be less than 6 mAh/g.

5.4. **Conclusions**

In summary, we have developed a simple two-step CVD method to synthesize hybrid CNF/HBGNs for LIB application. The lithium insertion behavior of the CNF/HBGN was studied. Using CNF/HBGNs as anode materials leads to a higher Li storage capability compared to CNF alone. The HBGNs with nanoporous cavities, large surface area, and edges of exposed graphene platelets provide not only more sites for Li-ions to be stored, but also high electrical conductivity and chemical stability. Moreover, the covalently bonded hybrid structure and substrate-bound CNFs provide fast ion/electron transfer. The hybrid material shows a reversible capacity of 300 mAh/g with excellent cycling stability. Higher purity and higher degree of graphitization of as-produced CNFs may be achieved by further chemical and thermal treatment, improving the charge capacity of CNFs, thus overall charge capacity of the hybrid is also expected to increase. With its large surface area and good electrical conductivity, this unique hybrid structure is also promising for supercapacitor applications. Our synthesis methods using PECVD provide a new technique for the design and synthesis of hybrid materials for versatile applications. In addition, commercially available, low cost CNFs will make the fabrication process readily scalable.

CHAPTER 6 CONCLUSIONS AND FUTURE DIRECTIONS

6.1. **Conclusions**

We introduced reliable ways to fabricate the hybrid materials and studied the various factors on the design of the electrode materials. The hybrid anode materials based on Si thin films and substrate-bound carbon nanostructures were designed and tested for the electrochemical performance. The novel hybrid nanomaterials demonstrated excellent cycle performance with a high energy density. Due to the unique structure of substrate-bound support materials and Si films, not only was the cycle life of the batteries greatly improved by the strong mechanical support, these new anodes also delivered a high lithium storage capacity. Furthermore, by eliminating the use of inactive materials such as a polymeric binder and conductive additives, the total weight of the battery system will decrease, which results in a higher energy density. This study led us to better understand the fundamental properties of the hybrid Si film/carbon nanostructure as an anode in LIBs. The hybrid CNF/HBGN also provided insights for fabricating the new class of carbon-carbon composites.

6.1.1 Hybrid electrode of Si thin film/HBGN (Si/HBGN)

A new graphene-based hybrid nanostructure has been designed for anode materials in LIBs. The HBGNs directly grown on a CVD-grown graphene film using dc PECVD under atmospheric pressure delivered promising electrochemical performance due to a network of highly conductive graphene nanosheets with a high density, a large surface area, and a high porosity. The hybrid graphene–HBGN structure was successfully designed to maintain its integral structure after long cycles. A charge capacity of 500 mAh/g at a current density of C/5 was obtained with 10% irreversible capacity loss after 100 cycles. The HBGN electrode retained a good charge capacity of 297 mAh/g, even at a high rate of 4 C. The synthesis procedure of the additive-free HBGN electrode was fairly simple, energy-efficient, and applicable for any conductive substrate, and thus promising for large-scale applications. Due to their unique morphology and structure, HBGNs have great potential as a supporting matrix in composite materials for active materials such as metal-based (Si/Si/Al/Sb) or transition-metal oxide nanoparticles, as well as host materials for Li-ions. We applied Si thin films on the substrate-bound HBGNs by LPCVD using SiH_4. The hybrid materials exhibited about 1,000 mAh/g over 100 cycles at the current rate of 1 C. We also demonstrated that the appropriate pore space was required for the silicon films to undergo large volume changes without significant degradation of battery performance.

6.1.2 Hybrid electrode of Si thin film/carbon nanofiber (Si/CNF)

The novel Si thin film/CNF hybrid materials were obtained by a two-step CVD method.

CNFs were directly grown on a stainless steel substrate as a supporting matrix for Si films; subsequently, the LPCVD method was used to deposit Si thin films on CNFs. The as-prepared Si/CNF hybrid materials on stainless steel were used for an anode without further treatment. The specific capacity of the CNFs was about 200 mAh/g, much smaller than that of hybrid Si/CNF electrodes; however, the CNFs showed very stable cycle performance without degradation of capacity after 150 cycles. The hybrid materials took advantage of the large surface area of CNFs and the high energy density of Si films. The hybrid Si/CNF exhibited a highly reversible capacity of about 1,000 mAh/g over 200 cycles and 66 % CE in the first cycle. The poor capacity retention of Si electrodes was addressed by combining the advantageous features of CNFs and Si film: (1) a strong mechanical structure for extended cycle performance, (2) efficient pathways for lithium-ion diffusion and electron transfer, and (3) stress-resistant Si thin film with excellent cycle stability. The electrochemical results were very promising and this study provided a possible approach for practical LIB anodes.

6.1.3 Hybrid electrode of carbon nanofiber/highly branched graphene nanosheet (CNF/HBGN)

The novel hybrid CNF/HBGN was synthesized via a simple two-step CVD method for anode materials in LIBs. First, we grew CNFs on a type 304 stainless steel without adding catalysts; subsequently, HBGN was grown on the surface of CNFs. Compared with the loosely bound hybrids prepared by the mechanical mixing of two materials or catalytic growth on graphene surface, the hybrid CNF/HBGN provided a continuous conduction pathway, which is expected to lead to a high charge carrier mobility. The CNFs offered a good electrical conductivity and a robust supporting structure, while the HBGNs provided increased Li storage sites. The hybrid CNF/HBGN as an anode material led to higher Li storage capability compared with CNF alone. The hybrid material showed a reversible capacity of 300 mAh/g with excellent cycling stability. The HBGNs with nanoporous cavities, large surface area, and edges of exposed graphene platelets provided more sites for Li-ion storage. Our synthesis methods using PECVD provided a new technique for the design and synthesis of hybrid materials for versatile applications. The controlled synthesis method of hybrid CNF/HBGN will offer insights into bottom-up design of carbon-carbon bond formation.

6.2. Future Directions

Further studies to better design the electrode materials are suggested as follows:

(1) **Reducing oxygen functional groups in carbon nanostructures:** A simple and efficient method of synthesizing substrate-bound carbon nanostructure is demonstrated. However, the main issue is the large irreversible capacity in the first cycle, which may be

associated with the irreversible reaction of Li-ions with oxygen functional groups present in the nanocarbon. The water-assisted synthesis method generates a large number of adsorbed oxygen species on the carbon nanostructure. Further study will be needed to reduce the oxygen species on the carbon nanostructure to improve the electrical conductivity and the capacity retention.

(2) **Improving the adhesion between Si films and carbon nanostructures**: The strong adhesion force between Si thin films and substrate-bound carbon nanostructures is essential for good cycle performance. The delamination of Si films from the substrate after repeated charge/discharge cycles may cause dramatic capacity fading. The effect of surface modification (e.g., changing roughness) of carbon nanostructure on the adhesion force of Si films will be a valuable aspect for improved cycle life of LIBs.

(3) **Controlled synthesis of carbon nanostructures:** The synthesis of carbon nanostructures with controlled void space will be required to effectively accommodate the large volume change of Si. Future study is warranted to understand the controllability of the carbon nanostructure configuraiton.

(4) **Stable solid-electrolyte interphase formation:** The huge volume change in Si leads to an unstable solid-electrolyte interphase (SEI) formation by disintegrating the SEI layer and exposing new Si surfaces to the electrolyte continually after repeated charge/discharge cycles. As a result, a thick SEI layer is formed, which increases the

electronic resistivity, and thus decreases the charge capacity due to the slow Li-ion transport. New design concepts for stable interphase between the electrolyte and the hybrid Si-C should be pursued.

ACKNOWLEDGEMENTS

I extend my deepest gratitude to everyone who supported my work during my Ph.D. study. Looking back on my five years at UWM, I have been very lucky to have wonderful teachers and friends. Above all, I extend my deepest gratitude to my advisor, Dr. Junhong Chen, who has provided me with insights, guidance, and support throughout my study. I also thank my committee members, Dr. Ying Li, Dr. Chris Yuan, Dr. Peter Hallac, and Dr. Benjamin Church for their support and valuable discussion.

I also thank the Power Solutions Division at Johnson Controls, Inc. for its financial support and valuable discussion, and great friends in Dr. Chen's research group; in particular, Dr. Xingkang Huang and Dr. Zhenhai Wen have provided valuable ideas and advices on the Li-ion battery research.

I extend my deep gratitude to my parents, my sister, and my brother, who have been always supportive and encouraging during my Ph.D. study. Finally, I heartily thank my beloved wife, Wen Luo. Without her support and encouragement, this dissertation would not have been possible. I owe special thanks to my two little girls, Hyewon and Jiwon, for their love and smiles.

References

1. Fauteux, D. and R. Koksbang, *Rechargeable lithium battery anodes: alternatives to metallic lithium.* Journal of applied electrochemistry, 1993. **23**(1): p. 1-10.
2. Landi, B.J., et al., *Carbon nanotubes for lithium ion batteries.* Energy & Environmental Science, 2009. **2**(6): p. 638-654.
3. Armand, M. and J.-M. Tarascon, *Building better batteries.* Nature, 2008. **451**(7179): p. 652-657.
4. Doughty, D., *Materials issues in lithium ion rechargeable battery technology*, 1995, Sandia National Labs., Albuquerque, NM (United States).
5. Bard, A.J. and L.R. Faulkner, *Electrochemical methods: fundamentals and applications*. Vol. 2. 1980: Wiley New York.
6. Park, M., et al., *A review of conduction phenomena in Li-ion batteries.* Journal of power sources, 2010. **195**(24): p. 7904-7929.
7. Bruce, P.G., B. Scrosati, and J.M. Tarascon, *Nanomaterials for rechargeable lithium batteries.* Angewandte Chemie International Edition, 2008. **47**(16): p. 2930-2946.
8. Van Schalkwijk, W. and B. Scrosati, *Advances in lithium-ion batteries*2002: Plenum Publishing Corporation.
9. Yang, S., H. Song, and X. Chen, *Electrochemical performance of expanded mesocarbon microbeads as anode material for lithium-ion batteries.* Electrochemistry communications, 2006. **8**(1): p. 137-142.
10. Ahn, S., et al., *Development of high capacity, high rate lithium ion batteries utilizing metal fiber conductive additives.* Journal of power sources, 1999. **81**: p. 896-901.
11. Che, G., et al., *Carbon nanotubule membranes for electrochemical energy storage and production.* Nature, 1998. **393**(6683): p. 346-349.
12. Zhao, J., et al., *First-principles study of Li-intercalated carbon nanotube ropes.* Physical review letters, 2000. **85**(8): p. 1706-1709.
13. Meunier, V., et al., *Ab initio investigations of lithium diffusion in carbon nanotube systems.* Physical review letters, 2002. **88**(7): p. 075506.
14. Yang, Z., et al., *Effects of doped copper on electrochemical performance of the raw carbon nanotubes anode.* Materials Letters, 2003. **57**(21): p. 3160-3166.
15. Lee, R., et al., *Conductivity enhancement in single-walled carbon nanotube bundles doped with K and Br.* Nature, 1997. **388**(6639): p. 255-257.
16. Huang, Z., et al., *Growth of highly oriented carbon nanotubes by plasma-enhanced hot filament chemical vapor deposition.* Applied physics letters, 1998. **73**(26): p. 3845-3847.

17. Guo, T., et al., *Self-assembly of tubular fullerenes.* The Journal of Physical Chemistry, 1995. **99**(27): p. 10694-10697.
18. Kong, J., A.M. Cassell, and H. Dai, *Chemical vapor deposition of methane for single-walled carbon nanotubes.* Chemical Physics Letters, 1998. **292**(4): p. 567-574.
19. Yang, S., et al., *Electrochemical performance of arc-produced carbon nanotubes as anode material for lithium-ion batteries.* Electrochimica acta, 2007. **52**(16): p. 5286-5293.
20. Gao, B., et al., *Enhanced saturation lithium composition in ball-milled single-walled carbon nanotubes.* Chemical Physics Letters, 2000. **327**(1): p. 69-75.
21. Zhang, H.X., et al., *Cross‐Stacked Carbon Nanotube Sheets Uniformly Loaded with SnO2 Nanoparticles: A Novel Binder‐Free and High‐Capacity Anode Material for Lithium‐Ion Batteries.* Advanced Materials, 2009. **21**(22): p. 2299-2304.
22. Chew, S.Y., et al., *Flexible free-standing carbon nanotube films for model lithium-ion batteries.* Carbon, 2009. **47**(13): p. 2976-2983.
23. Geim, A.K. and K.S. Novoselov, *The rise of graphene.* Nature materials, 2007. **6**(3): p. 183-191.
24. Gusynin, V. and S. Sharapov, *Unconventional integer quantum Hall effect in graphene.* Physical review letters, 2005. **95**(14): p. 146801.
25. Zhang, Y., et al., *Experimental observation of the quantum Hall effect and Berry's phase in graphene.* Nature, 2005. **438**(7065): p. 201-204.
26. Lin, Y.-M., et al., *100-GHz transistors from wafer-scale epitaxial graphene.* Science, 2010. **327**(5966): p. 662-662.
27. Hwang, E., S. Adam, and S.D. Sarma, *Carrier transport in two-dimensional graphene layers.* Physical review letters, 2007. **98**(18): p. 186806.
28. Yoo, E., et al., *Large reversible Li storage of graphene nanosheet families for use in rechargeable lithium ion batteries.* Nano letters, 2008. **8**(8): p. 2277-2282.
29. Zhao, X., et al., *In‐Plane Vacancy‐Enabled High‐Power Si–Graphene Composite Electrode for Lithium‐Ion Batteries.* Advanced Energy Materials, 2011. **1**(6): p. 1079-1084.
30. Dey, A., *Electrochemical alloying of lithium in organic electrolytes.* Journal of The Electrochemical Society, 1971. **118**(10): p. 1547-1549.
31. Boukamp, B., G. Lesh, and R. Huggins, *All‐solid lithium electrodes with mixed‐conductor matrix.* Journal of The Electrochemical Society, 1981. **128**(4): p. 725-729.
32. Chan, C.K., et al., *High-performance lithium battery anodes using silicon nanowires.* Nature nanotechnology, 2007. **3**(1): p. 31-35.

33. Ryu, J.H., et al., *Failure modes of silicon powder negative electrode in lithium secondary batteries.* Electrochemical and solid-state letters, 2004. **7**(10): p. A306-A309.
34. Wilson, A. and J. Dahn, *Lithium insertion in carbons containing nanodispersed silicon.* Journal of The Electrochemical Society, 1995. **142**(2): p. 326-332.
35. Kasavajjula, U., C. Wang, and A.J. Appleby, *Nano-and bulk-silicon-based insertion anodes for lithium-ion secondary cells.* Journal of power sources, 2007. **163**(2): p. 1003-1039.
36. Liu, X.H., et al., *Size-dependent fracture of silicon nanoparticles during lithiation.* Acs Nano, 2012. **6**(2): p. 1522-1531.
37. Li, H., et al., *Research on Advanced Materials for Li‐ion Batteries.* Advanced Materials, 2009. **21**(45): p. 4593-4607.
38. Song, T., et al., *Arrays of sealed silicon nanotubes as anodes for lithium ion batteries.* Nano letters, 2010. **10**(5): p. 1710-1716.
39. Cui, L.-F., et al., *Crystalline-amorphous core− shell silicon nanowires for high capacity and high current battery electrodes.* Nano letters, 2008. **9**(1): p. 491-495.
40. Maranchi, J., A. Hepp, and P. Kumta, *High capacity, reversible silicon thin-film anodes for lithium-ion batteries.* Electrochemical and solid-state letters, 2003. **6**(9): p. A198-A201.
41. Takamura, T., et al., *A vacuum deposited Si film having a Li extraction capacity over 2000 mAh/g with a long cycle life.* Journal of power sources, 2004. **129**(1): p. 96-100.
42. Fleischauer, M., J. Li, and M. Brett, *Columnar thin films for three-dimensional microbatteries.* Journal of The Electrochemical Society, 2009. **156**(1): p. A33-A36.
43. Graetz, J., et al., *Highly reversible lithium storage in nanostructured silicon.* Electrochemical and Solid-State Letters, 2003. **6**(9): p. A194-A197.
44. Hu, L., et al., *Si nanoparticle-decorated Si nanowire networks for Li-ion battery anodes.* Chemical Communications, 2011. **47**(1): p. 367-369.
45. Kim, H., et al., *Three‐Dimensional Porous Silicon Particles for Use in High‐Performance Lithium Secondary Batteries.* Angewandte Chemie, 2008. **120**(52): p. 10305-10308.
46. Cho, J., *Porous Si anode materials for lithium rechargeable batteries.* Journal of Materials Chemistry, 2010. **20**(20): p. 4009-4014.
47. Chan, C.K., et al., *High-performance lithium battery anodes using silicon nanowires.* Nature nanotechnology, 2008. **3**(1): p. 31-35.
48. Gu, P., et al., *Si/C composite lithium-ion battery anodes synthesized from coarse silicon and citric acid through combined ball milling and thermal pyrolysis.* Electrochimica acta, 2010. **55**(12): p. 3876-3883.

49. Wang, W., R. Epur, and P.N. Kumta, *Vertically aligned silicon/carbon nanotube (VASCNT) arrays: hierarchical anodes for lithium-ion battery.* Electrochemistry communications, 2011. **13**(5): p. 429-432.
50. Zhou, X., et al., *Spin-coated silicon nanoparticle/graphene electrode as a binder-free anode for high-performance lithium-ion batteries.* Nano Research, 2012. **5**(12): p. 845-853.
51. Chang, J., et al., *Multilayered Si Nanoparticle/Reduced Graphene Oxide Hybrid as a High‐Performance Lithium‐Ion Battery Anode.* Advanced Materials, 2013.
52. Wang, J.-Z., et al., *Flexible free-standing graphene-silicon composite film for lithium-ion batteries.* Electrochemistry communications, 2010. **12**(11): p. 1467-1470.
53. Wang, B., et al., *Adaptable silicon–carbon nanocables sandwiched between reduced graphene oxide sheets as lithium ion battery anodes.* ACS nano, 2013. **7**(2): p. 1437-1445.
54. Liu, B., et al., *Hierarchical silicon nanowires-carbon textiles matrix as a binder-free anode for high-performance advanced lithium-ion batteries.* Scientific reports, 2013. **3**.
55. Cui, L.-F., et al., *Carbon− silicon core− shell nanowires as high capacity electrode for lithium ion batteries.* Nano letters, 2009. **9**(9): p. 3370-3374.
56. Evanoff, K., et al., *Ultra strong silicon-coated carbon nanotube nonwoven fabric as a multifunctional lithium-ion battery anode.* ACS nano, 2012. **6**(11): p. 9837-9845.
57. Cui, L.-F., et al., *Light-weight free-standing carbon nanotube-silicon films for anodes of lithium ion batteries.* ACS nano, 2010. **4**(7): p. 3671-3678.
58. Kang, B. and G. Ceder, *Battery materials for ultrafast charging and discharging.* Nature, 2009. **458**(7235): p. 190-193.
59. Tarascon, J. and M. Armand, *Issues and challenges facing rechargeable lithium batteries.* Nature, 2001. **414**: p. 359-367.
60. Yang, L., et al., *Mesoporous germanium as anode material of high capacity and good cycling prepared by a mechanochemical reaction.* Electrochemistry Communications, 2010. **12**(3): p. 418-421.
61. Wu, Y., et al., *Preparation of carbon coated MoO2 nanobelts and their high performance as anode materials for lithium ion batteries.* Journal of Materials Chemistry, 2012.
62. Dahn, J., et al., *Mechanisms for lithium insertion in carbonaceous materials.* Science, 1995. **270**(5236): p. 590.
63. Noel, M. and V. Suryanarayanan, *Role of carbon host lattices in Li-ion intercalation/de-intercalation processes.* Journal of power sources, 2002. **111**(2):

p. 193-209.
64. Buqa, H., et al., *High rate capability of graphite negative electrodes for lithium-ion batteries.* Journal of the Electrochemical Society, 2005. **152**: p. A474.
65. Kaskhedikar, N.A. and J. Maier, *Lithium storage in carbon nanostructures.* Advanced Materials, 2009. **21**(25 26): p. 2664-2680.
66. Novoselov, K., et al., *Two-dimensional gas of massless Dirac fermions in graphene.* Nature, 2005. **438**(7065): p. 197-200.
67. Stankovich, S., et al., *Graphene-based composite materials.* Nature, 2006. **442**(7100): p. 282-286.
68. Lee, C., et al., *Measurement of the elastic properties and intrinsic strength of monolayer graphene.* Science, 2008. **321**(5887): p. 385-388.
69. Guo, P., H. Song, and X. Chen, *Electrochemical performance of graphene nanosheets as anode material for lithium-ion batteries.* Electrochemistry Communications, 2009. **11**(6): p. 1320-1324.
70. Yoo, E.J., et al., *Large reversible Li storage of graphene nanosheet families for use in rechargeable lithium ion batteries.* Nano letters, 2008. **8**(8): p. 2277-2282.
71. Wang, G., et al., *Graphene nanosheets for enhanced lithium storage in lithium ion batteries.* Carbon, 2009. **47**(8): p. 2049-2053.
72. Lian, P., et al., *Large reversible capacity of high quality graphene sheets as an anode material for lithium-ion batteries.* Electrochimica Acta, 2010. **55**(12): p. 3909-3914.
73. Wang, D., et al., *Self-assembled TiO2–graphene hybrid nanostructures for enhanced Li-ion insertion.* ACS nano, 2009. **3**(4): p. 907-914.
74. Evanoff, K., et al., *Nanosilicon‐Coated Graphene Granules as Anodes for Li‐Ion Batteries.* Advanced Energy Materials, 2011. **1**(4): p. 495-498.
75. Liang, M. and L. Zhi, *Graphene-based electrode materials for rechargeable lithium batteries.* J. Mater. Chem., 2009. **19**(33): p. 5871-5878.
76. Chen, Z., et al., *Three-dimensional flexible and conductive interconnected graphene networks grown by chemical vapour deposition.* Nature materials, 2011. **10**(6): p. 424-428.
77. Wu, Y., et al., *Carbon nanowalls grown by microwave plasma enhanced chemical vapor deposition.* Advanced Materials, 2002. **14**(1): p. 64-67.
78. Tanaike, O., et al., *Lithium insertion behavior of carbon nanowalls by dc plasma CVD and its heat-treatment effect.* Solid State Ionics, 2009. **180**(4-5): p. 381-385.
79. Xiao, X., et al., *Vertically aligned graphene electrode for lithium ion battery with high rate capability.* Electrochemistry Communications, 2011. **13**(2): p. 209-212.
80. Yu, K., et al., *Growth of carbon nanowalls at atmospheric pressure for one-step gas sensor fabrication.* Nanoscale Research Letters, 2011. **6**(1): p. 202.
81. Yu, K., et al., *Patterning Vertically Oriented Graphene Sheets for Nanodevice*

Applications. The Journal of Physical Chemistry Letters, 2011. **2**(6): p. 537-542.
82. Bo, Z., et al., *Vertically oriented graphene sheets grown on metallic wires for greener corona discharges: lower power consumption and minimized ozone emission*. Energy & Environmental Science, 2011. **49**(6): p. 1849-1858.
83. Yu, K., et al., *Carbon Nanotube with Chemically-bonded Graphene Leaves for Electronic and Optoelectronic Applications*. The Journal of Physical Chemistry Letters, 2011. **2**(13): p. 1556-1562.
84. Reina, A., et al., *Large area, few-layer graphene films on arbitrary substrates by chemical vapor deposition*. Nano letters, 2008. **9**(1): p. 30-35.
85. Bo, Z., et al., *Understanding growth of carbon nanowalls at atmospheric pressure using normal glow discharge plasma-enhanced chemical vapor deposition*. Carbon, 2011. **49**(6): p. 1849-1858.
86. Wu, Y.P., et al., *Mechanism of lithium storage in low temperature carbon*. Carbon, 1999. **37**(12): p. 1901-1908.
87. Dahn, J., W. Xing, and Y. Gao, *The "falling cards model" for the structure of microporous carbons*. Carbon, 1997. **35**(6): p. 825-830.
88. Xing, W. and J. Dahn, *Study of irreversible capacities for Li insertion in hard and graphitic carbons*. Journal of the Electrochemical Society, 1997. **144**: p. 1195.
89. Yazami, R. and M. Deschamps, *High reversible capacity carbon-lithium negative electrode in polymer electrolyte*. Journal of power sources, 1995. **54**(2): p. 411-415.
90. Jamnik, J. and J. Maier, *Treatment of the Impedance of Mixed Conductors Equivalent Circuit Model and Explicit Approximate Solutions*. Journal of the Electrochemical Society, 1999. **146**: p. 4183.
91. Magasinski, A., et al., *High-performance lithium-ion anodes using a hierarchical bottom-up approach*. Nature materials, 2010. **9**(4): p. 353-358.
92. Wu, H., et al., *Stable Li-ion battery anodes by in-situ polymerization of conducting hydrogel to conformally coat silicon nanoparticles*. Nature communications, 2013. **4**.
93. Chang, J., et al., *Lithium‐Ion Batteries: Multilayered Si Nanoparticle/Reduced Graphene Oxide Hybrid as a High‐Performance Lithium‐Ion Battery Anode (Adv. Mater. 5/2014)*. Advanced Materials, 2014. **26**(5): p. 665-665.
94. Wang, W. and P.N. Kumta, *Nanostructured hybrid silicon/carbon nanotube heterostructures: reversible high-capacity lithium-ion anodes*. ACS nano, 2010. **4**(4): p. 2233-2241.
95. Chen, P.-C., et al., *Hybrid silicon-carbon nanostructured composites as superior anodes for lithium ion batteries*. Nano Research, 2011. **4**(3): p. 290-296.
96. Luo, J., et al., *Crumpled graphene-encapsulated Si nanoparticles for lithium ion battery anodes*. The Journal of Physical Chemistry Letters, 2012. **3**(13): p.

1824-1829.
97. Xiang, H., et al., *Graphene/nanosized silicon composites for lithium battery anodes with improved cycling stability.* Carbon, 2011. **49**(5): p. 1787-1796.
98. Kim, H., et al., *Straightforward fabrication of a highly branched graphene nanosheet array for a Li-ion battery anode.* Journal of Materials Chemistry, 2012. **22**(31): p. 15514-15518.
99. Zhou, X., et al., *Facile synthesis of silicon nanoparticles inserted into graphene sheets as improved anode materials for lithium-ion batteries.* Chemical Communications, 2012. **48**(16): p. 2198-2200.
100. Lee, J.K., et al., *Silicon nanoparticles–graphene paper composites for Li ion battery anodes.* Chemical Communications, 2010. **46**(12): p. 2025-2027.
101. Yu, K., et al., *Growth of carbon nanowalls at atmospheric pressure for one-step gas sensor fabrication.* Nanoscale research letters, 2011. **6**(1): p. 1-9.
102. Yu, K., et al., *Patterning vertically oriented graphene sheets for nanodevice applications.* The Journal of Physical Chemistry Letters, 2011. **2**(6): p. 537-542.
103. Ng, S.H., et al., *Highly Reversible Lithium Storage in Spheroidal Carbon‐Coated Silicon Nanocomposites as Anodes for Lithium‐Ion Batteries.* Angewandte Chemie International Edition, 2006. **45**(41): p. 6896-6899.
104. Dimov, N., S. Kugino, and M. Yoshio, *Carbon-coated silicon as anode material for lithium ion batteries: advantages and limitations.* Electrochimica acta, 2003. **48**(11): p. 1579-1587.
105. Beattie, S.D., et al., *Si electrodes for Li-ion batteries—a new way to look at an old problem.* Journal of The Electrochemical Society, 2008. **155**(2): p. A158-A163.
106. Renner, O. and J. Zemek, *Density of amorphous silicon films.* Czechoslovak Journal of Physics, 1973. **23**(11): p. 1273-1276.
107. Aricò, A.S., et al., *Nanostructured materials for advanced energy conversion and storage devices.* Nature materials, 2005. **4**(5): p. 366-377.
108. Wu, H., et al., *Engineering empty space between Si nanoparticles for lithium-ion battery anodes.* Nano letters, 2012. **12**(2): p. 904-909.
109. Park, M.-H., et al., *Silicon nanotube battery anodes.* Nano letters, 2009. **9**(11): p. 3844-3847.
110. Wu, H., et al., *Stable cycling of double-walled silicon nanotube battery anodes through solid-electrolyte interphase control.* Nature nanotechnology, 2012. **7**(5): p. 310-315.
111. Chan, C.K., et al., *Solution-grown silicon nanowires for lithium-ion battery anodes.* ACS nano, 2010. **4**(3): p. 1443-1450.
112. Peng, K., et al., *Silicon nanowires for rechargeable lithium-ion battery anodes.* Applied physics letters, 2008. **93**(3): p. 033105.
113. Abel, P.R., et al., *Improving the stability of nanostructured silicon thin film*

lithium-ion battery anodes through their controlled oxidation. ACS nano, 2012. **6**(3): p. 2506-2516.

114. Lee, K.-L., et al., *Electrochemical characteristics of a-Si thin film anode for Li-ion rechargeable batteries.* Journal of power sources, 2004. **129**(2): p. 270-274.
115. Hatalis, M.K. and D.W. Greve, *Large grain polycrystalline silicon by low‐temperature annealing of low‐pressure chemical vapor deposited amorphous silicon films.* Journal of applied physics, 1988. **63**(7): p. 2260-2266.
116. Baranchugov, V., et al., *Amorphous silicon thin films as a high capacity anodes for Li-ion batteries in ionic liquid electrolytes.* Electrochemistry communications, 2007. **9**(4): p. 796-800.
117. Uehara, M., et al., *Thick vacuum deposited silicon films suitable for the anode of Li-ion battery.* Journal of power sources, 2005. **146**(1): p. 441-444.
118. Evanoff, K., et al., *Towards ultrathick battery electrodes: Aligned carbon nanotube–enabled architecture.* Advanced Materials, 2012. **24**(4): p. 533-537.
119. Baddour, C.E., et al., *A simple thermal CVD method for carbon nanotube synthesis on stainless steel 304 without the addition of an external catalyst.* Carbon, 2009. **47**(1): p. 313-318.
120. Martin-Gullon, I., et al., *Differences between carbon nanofibers produced using Fe and Ni catalysts in a floating catalyst reactor.* Carbon, 2006. **44**(8): p. 1572-1580.
121. Rodriguez, N.M., A. Chambers, and R.T.K. Baker, *Catalytic engineering of carbon nanostructures.* Langmuir, 1995. **11**(10): p. 3862-3866.
122. Masarapu, C. and B. Wei, *Direct growth of aligned multiwalled carbon nanotubes on treated stainless steel substrates.* Langmuir, 2007. **23**(17): p. 9046-9049.
123. Sinnott, S., et al., *Model of carbon nanotube growth through chemical vapor deposition.* Chemical Physics Letters, 1999. **315**(1): p. 25-30.
124. Kukovitsky, E., et al., *Correlation between metal catalyst particle size and carbon nanotube growth.* Chemical Physics Letters, 2002. **355**(5): p. 497-503.
125. Yoshio, M., et al., *Carbon-coated Si as a lithium-ion battery anode material.* Journal of The Electrochemical Society, 2002. **149**(12): p. A1598-A1603.
126. Magasinski, A., et al., *Toward efficient binders for Li-ion battery Si-based anodes: polyacrylic acid.* ACS applied materials & interfaces, 2010. **2**(11): p. 3004-3010.
127. Freund, L.B. and S. Suresh, *Thin film materials: stress, defect formation and surface evolution*2003: Cambridge University Press.
128. Pharr, M., Z. Suo, and J.J. Vlassak, *Measurements of the Fracture Energy of Lithiated Silicon Electrodes of Li-Ion Batteries.* Nano letters, 2013. **13**(11): p. 5570-5577.
129. Sethuraman, V.A., et al., *< i> In situ</i> measurements of stress evolution in silicon thin films during electrochemical lithiation and delithiation.* Journal of

power sources, 2010. **195**(15): p. 5062-5066.

130. Suo, Z., *Reliability of interconnect structures.* Volume, 2003. **8**: p. 265-324.
131. Griffith, A., *VI. The Phenomena of Rupture and F low in Solids.* Phil. Trans. Roy. Soc.(Lon.) A, 1920. **221**: p. 163-198.
132. Wang, J.W., et al., *Sandwich-lithiation and longitudinal crack in amorphous silicon coated on carbon nanofibers.* ACS nano, 2012. **6**(10): p. 9158-9167.
133. Vajtai, R., *Springer Handbook of Nanomaterials*2013: Springer.
134. Fan, Z., et al., *A Three‐Dimensional Carbon Nanotube/Graphene Sandwich and Its Application as Electrode in Supercapacitors.* Advanced Materials, 2010. **22**(33): p. 3723-3728.
135. Tung, V.C., et al., *Low-temperature solution processing of graphene− carbon nanotube hybrid materials for high-performance transparent conductors.* Nano letters, 2009. **9**(5): p. 1949-1955.
136. Yu, D. and L. Dai, *Self-assembled graphene/carbon nanotube hybrid films for supercapacitors.* The Journal of Physical Chemistry Letters, 2009. **1**(2): p. 467-470.
137. Lee, D.H., et al., *Versatile carbon hybrid films composed of vertical carbon nanotubes grown on mechanically compliant graphene films.* Advanced Materials, 2010. **22**(11): p. 1247-1252.
138. Li, S., et al., *Vertically Aligned Carbon Nanotubes Grown on Graphene Paper as Electrodes in Lithium‐Ion Batteries and Dye‐Sensitized Solar Cells.* Advanced Energy Materials, 2011. **1**(4): p. 486-490.
139. Novoselov, K.S., et al., *A roadmap for graphene.* Nature, 2012. **490**(7419): p. 192-200.
140. Novoselov, K., et al., *Two-dimensional gas of massless Dirac fermions in graphene.* Nature, 2005. **438**(7065): p. 197-200.
141. Li, X., et al., *Large-area synthesis of high-quality and uniform graphene films on copper foils.* Science, 2009. **324**(5932): p. 1312-1314.
142. Neto, A.C., et al., *The electronic properties of graphene.* Reviews of modern physics, 2009. **81**(1): p. 109.
143. Du, X., et al., *Approaching ballistic transport in suspended graphene.* Nature nanotechnology, 2008. **3**(8): p. 491-495.
144. Areshkin, D.A., D. Gunlycke, and C.T. White, *Ballistic transport in graphene nanostrips in the presence of disorder: importance of edge effects.* Nano letters, 2007. **7**(1): p. 204-210.
145. Dean, C., et al., *Boron nitride substrates for high-quality graphene electronics.* Nature nanotechnology, 2010. **5**(10): p. 722-726.
146. Lee, J.H., et al., *One‐Step Exfoliation Synthesis of Easily Soluble Graphite and Transparent Conducting Graphene Sheets.* Advanced Materials, 2009. **21**(43): p.

4383-4387.

147. Berger, C., et al., *Electronic confinement and coherence in patterned epitaxial graphene.* Science, 2006. **312**(5777): p. 1191-1196.
148. Emtsev, K.V., et al., *Towards wafer-size graphene layers by atmospheric pressure graphitization of silicon carbide.* Nature materials, 2009. **8**(3): p. 203-207.
149. Kuang, Q., et al., *Low temperature solvothermal synthesis of crumpled carbon nanosheets.* Carbon, 2004. **42**(8): p. 1737-1741.
150. Gomez De Arco, L., et al., *Continuous, highly flexible, and transparent graphene films by chemical vapor deposition for organic photovoltaics.* ACS nano, 2010. **4**(5): p. 2865-2873.
151. Bae, S., et al., *Roll-to-roll production of 30-inch graphene films for transparent electrodes.* Nature nanotechnology, 2010. **5**(8): p. 574-578.
152. Eda, G., G. Fanchini, and M. Chhowalla, *Large-area ultrathin films of reduced graphene oxide as a transparent and flexible electronic material.* Nature nanotechnology, 2008. **3**(5): p. 270-274.
153. Bonaccorso, F., et al., *Graphene photonics and optoelectronics.* Nature Photonics, 2010. **4**(9): p. 611-622.
154. Dua, V., et al., *All‐Organic Vapor Sensor Using Inkjet‐Printed Reduced Graphene Oxide.* Angewandte Chemie International Edition, 2010. **49**(12): p. 2154-2157.
155. Mao, S., et al., *Tuning gas-sensing properties of reduced graphene oxide using tin oxide nanocrystals.* J. Mater. Chem., 2012. **22**(22): p. 11009-11013.
156. Pumera, M., *Graphene-based nanomaterials for energy storage.* Energy & Environmental Science, 2011. **4**(3): p. 668-674.
157. Wen, Z., et al., *Crumpled Nitrogen‐Doped Graphene Nanosheets with Ultrahigh Pore Volume for High‐Performance Supercapacitor.* Advanced Materials, 2012. **24**(41): p. 5610-5616.
158. Mao, S., et al., *A general approach to one-pot fabrication of crumpled graphene-based nanohybrids for energy applications.* ACS nano, 2012. **6**(8): p. 7505-7513.
159. Chae, S.H., et al., *Transferred wrinkled Al2O3 for highly stretchable and transparent graphene–carbon nanotube transistors.* Nature materials, 2013. **12**(5): p. 403-409.
160. Kim, K.H., Y. Oh, and M. Islam, *Graphene coating makes carbon nanotube aerogels superelastic and resistant to fatigue.* Nature nanotechnology, 2012. **7**(9): p. 562-566.
161. Yu, K., et al., *Carbon nanotube with chemically bonded graphene leaves for electronic and optoelectronic applications.* The Journal of Physical Chemistry Letters, 2011. **2**(13): p. 1556-1562.

162. Casiraghi, C., et al., *Raman spectroscopy of graphene edges.* Nano letters, 2009. **9**(4): p. 1433-1441.
163. Lorang, G., et al., *Chemical composition of passive films on AISI 304 stainless steel.* Journal of The Electrochemical Society, 1994. **141**(12): p. 3347-3356.

CURRICULUM VITAE

Haejune Kim

EDUCATION:

Ph. D. candidate in Mechanical Engineering
University of Wisconsin-Milwaukee, Milwaukee, WI
Expected Grad: 08/2014 GPA: 3.9 out of 4.0

Master of Science in Mechanical Engineering
Texas A&M University, College Station, TX
Grad: 08/2007 GPA: 3.6 out of 4.0

Bachelor of Science in Mechanical Engineering
Korea University, Seoul, Korea
Grad: 02/2004 GPA: 3.9 out of 4.5

WORK EXPERIENCE:

Texas A&M University
Technical Lab Manager
College Station, TX 01/2014 – present

- Maintained lab equipment and supplies inventory at shared service facility in the department of Mechanical Engineering and provided technical support and training

A.O. Smith Corporation Technology Center
Mechanical Engineering Intern
Milwaukee, WI 05/2013- 12/2013

- Evaluated efficiency improvement of thermoelectric devices in electric water heaters
- Developed heat recovery modules based on a heat pipe-heat exchanger

Advanced Test Concepts (ATC), Inc
Research Engineer
Indianapolis, IN 03/2008 – 01/2009

- Led a product development team for new product development
- Designed and conducted leak testing of various mechanical components for the seal integrity
- Performed mechanical design for new products using SolidWorks

- Designed experiments and conducted data acquisition measurement via a LabVIEW-based leak measurement system

Korean Army
Helicopter Dispatcher
Chungnam, Korea 04/1999 – 06/2001

- Managed flight plans of 40 helicopters; supervised 8 assistants.
- Analyzed and evaluated meteorological information for flight safety.
- No accidents for 2 years; elected best helicopter unit.

CERTIFICATE Engineer in Training (EIT), 10/2012

PUBLICATIONS

(1) H. Kim, X. Huang, Z. H. Wen, S. M. Cui, and J. H. Chen, "Novel hybrid Si film/highly branched graphene nanosheet for anode materials in lithium-ion batteries," *Submitted to Chemical Communications*, 2014

(2) H. Kim, X. Huang, Z. H. Wen, S. M. Cui, and J. H. Chen, "Novel hybrid carbon nanofiber/highly branched graphene nanosheet for anode materials in lithium-ion batteries," *Submitted to ACS Applied Materials & Interfaces*, 2014

(3) H. Kim, X. Huang, Z. H. Wen, S. M. Cui, and J. H. Chen, "Novel hybrid Si film/carbon nanofiber for anode materials in lithium-ion batteries," *Submitted to Journal of Materials Chemicstry A*, 2014

(4) K. H. Yu, G. H. Lu, Z. H. Wen, H. Kim, Y. Y. Qian, E. Andrew, S. Mao, and J. H. Chen, "Hierarchical Vertically-Oriented Graphene as a Catalytic Counter Electrode in Dye-Sensitized Solar Cells," *Journal of Materials Chemistry*. 1, 188-193, 2013.

(5) Z. H. Wen, G. Lu, S. Mao, H. Kim, S. Cui, K. H. Yu, , X. Huang, P. Hurley, O. Mao, and J. H. Chen,"Silicon nanotube anode for lithium-ion batteries." *Electrochemistry Communications*, *29*, 67-70, 2013.

(6) S. Mao, Z. H. Wen, H. Kim, G. H. Lu, P. Hurley, and J. H. Chen, "A General Approach to One-Pot Fabrication of Crumpled Graphene-Based Nanohybrids for Energy Applications," *ACS Nano*. 6(8), 7505-7513, 2012.

(7) Z. H. Wen, X. C. Wang, S. Mao, Z. Bo, H. Kim, S. M. Cui, G. H. Lu, X. L. Feng, and J. H. Chen, “Crumpled Nitrogen-Doped Graphene Nanosheets with Ultrahigh Pore Volume for High-performance Supercapacitor,” *Advanced Materials*.24(41), 5610-5616, 2012.

(8) H. Kim, Z. H. Wen, K. H. Yu, O. Mao, and J. H. Chen, “Straightforward Fabrication of Highly Branched Graphene Nanosheet Array for Li-ion Battery Anode,” *Journal of Materials Chemistry*. 22(31), 15514-15518, 2012.

(9) Z. Bo, Z. H. Wen, H. Kim, G. Luo, K. H. Yu, and J. H. Chen, “One-step Fabrication and Capacitive Behavior of Electrochemical Double Layer Capacitor Electrodes Using Vertically-Oriented Graphene Directly Grown on Metal,” *Carbon*, *50*(12), 4379-4387, 2012.

(10) Z. H. Wen, S. M. Cui, H. Kim, S. Mao, K. H. Yu, G. H. Lu, H. H. Pu, O. Mao, and J. H. Chen, “Binding Sn-Based Nanoparticles on Graphene as Anode of Lithium Ions Batteries,” *Journal of Materials Chemistry*. 22(8), 3300-3306, 2012.

(11) K. H. Yu, G. H. Lu, K. H. Chen, S. Mao, H. Kim, and J. H. Chen, “Controllable Photoelectron Transfer in CdSe Nanocrystal-Carbon Nanotube Hybrid Structures,” *Nanoscale*. 4(3), 742-746, 2012.

(12) K. H. Yu, G. H. Lu, S. Mao, H. Kim, and J. H. Chen, “Selective Deposition of CdSe Nanoparticles on Reduced Graphene Oxide to Understand Photoinduced Charge Transfer in Hybrid Nanostructures,” *ACS Applied Materials & Interfaces*. 3(7), 2703-2709, 2011.

(13) H. Peng, H. Kim, D. Luo, M. Marquez, Z. Cheng, “Low-frequency ac electro-flow-focusing microfluidic emulsification,” *Applied Physics Letters*. 96, 174103, 2010.

(14) H. Kim, D. Luo, D. Link, D. Weitz,M. Marquez, Z. Cheng, “Controlled production of emulsion drops using An Electric Field in a Flow Focusing Microfluidic Device,” *Applied Physics Letters*. 91,133106, 2007.

AWARDS

Chancellor’s Award at University of Wisconsin-Milwaukee
Texas A&M University Engineering Scholarship
Dean’s Honor List at Korea University